

Chapter 6

## Experimental Reality of Geostrophic Adjustment

A. Stegner

*Laboratoire de Météorologie Dynamique, CNRS,  
ENS, 24, rue Lhomond, 75231 Paris Cedex 05, France*

### Contents

1. The Holy Graal of rotating shallow-water flows	325
1.1. Single layer $f$ -plane configuration	326
1.2. Influences of the centrifugal force	331
1.3. Non-hydrostatic wave modes	333
1.4. Two-layer stratification	336
2. Potential vorticity measurements: a new challenge	341
2.1. Particle image velocimetry and vorticity field measurements	342
2.2. Height field measurements	345
2.3. Potential vorticity measurements	352
3. Simple case studies of geostrophic adjustment	354
3.1. “Warm-core” lens	354
3.2. Cyclonic and anticyclonic PV patches	360
3.3. Uniform PV front	370
4. What do we learn from laboratory experiments?	377
Acknowledgements	378
Uncited references	378
References	379

### 1. The Holy Graal of rotating shallow-water flows

The rotating shallow water model (RSW) is probably the most pedagogical and useful model to understand geophysical fluid dynamics. Even if the RSW equations are based on drastic assumptions (hydrostatic balance, quasi-bidimensionality, weak dissipation) it is a surprisingly good model of many

1 phenomena in the atmosphere and the ocean. Nevertheless, as far as laboratory 1  
 2 experiments are concerned, one should keep in mind that the dynamics of a rotat- 2  
 3 ing and stratified fluid is given by the full three-dimensional Navier–Stokes 3  
 4 equations at the final place. As it was shown in Chapter 1, the RSW equations can 4  
 5 be derived from the primitive equations according to an asymptotic expansion 5  
 6 which indeed remains valid for some restricted range of dynamical parameters. 6  
 7 However, this derivation starts from the hydrostatic and non-dissipative primitive 7  
 8 equations (Chapter 1), while both hydrostatic and dissipative effects could play a 8  
 9 role in the laboratory. Hence, we recall in this section the derivation of the RSW 9  
 10 model from the Navier–Stokes equations. The main purpose is to understand here 10  
 11 which dynamical processes are filtered out by the RSW model while they occur 11  
 12 sometimes in real experiment. Moreover, we will try to specify the value of the 12  
 13 dynamical parameters needed to be achieved in laboratory experiments in order to 13  
 14 be close to the RSW dynamics. 14

15  
 16 *1.1. Single layer f-plane configuration* 16

17  
 18 Let us consider first a single barotropic and incompressible fluid layer in a rotating 18  
 19 tank with a flat bottom and a free upper surface, as shown in Figure 1. 19

20 In order to get a dimensionless set of equations we use:  $L$  and  $H_0$  as horizon- 20  
 21 tal and vertical scales,  $T$  the characteristic time-scale for the flow evolution,  $U$  21  
 22 and  $U(H_0/L)$  as horizontal and vertical velocity scales,  $\rho g H_0$  as the charac- 22  
 23 teristic hydrostatic pressure scale and  $\rho f UL$  the scale of pressure deviation from 23  
 24 hydrostatic balance ( $f = 2\Omega_0$  the Coriolis parameter). Using this dimensionless 24  
 25 formulation, the Navier–Stokes equations can be written as follows: 25

26  
 27 
$$\varepsilon \partial_t u + Ro \mathcal{D}u - v = -\partial_x \pi + E_k \Delta u, \tag{1}$$

28  
 29 
$$\varepsilon \partial_t v + Ro \mathcal{D}v + u = -\partial_y \pi + E_k \Delta v, \tag{2}$$

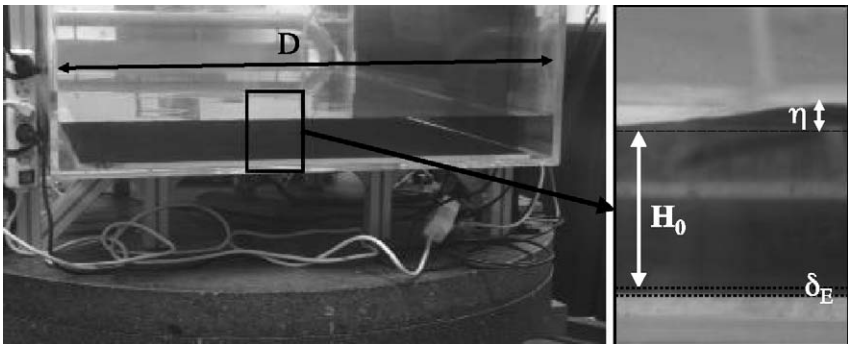


Figure 1. Single water layer on a rotating turntable  $H_0 = 10$  cm and  $D = 90$  cm.

$$\alpha^2[\varepsilon\partial_t w + Ro\mathcal{D}w] = -\partial_z\pi + \alpha^2 E_k \Delta w \quad (3)$$

where  $\mathcal{D} = u\partial_x + v\partial_y + w\partial_z$  and  $\Delta = \partial_{z^2} + \alpha^2(\partial_{x^2} + \partial_{y^2})$ . Besides, in this formulation we decouple the hydrostatic pressure  $P_H$  corresponding to the fluid at rest and the dynamical pressure  $\pi$  (pressure deviation induced by the fluid motion) according to:

$$P = P_H(z) + \frac{Ro}{Bu}\pi(x, y, z, t) \quad (4)$$

where  $P_H(z) = 1 - z + P_0$  and  $P_0$  is the dimensionless pressure at the free-surface.

In addition one should consider the continuity equation

$$\partial_x u + \partial_y v + \partial_z w = 0 \quad (5)$$

with upper ( $z_1 = 1 + \lambda\eta$ ) and lower ( $z_0 = 0$ ) boundary conditions:

$$u(z_0) = v(z_0) = w(z_0) = 0, \quad (6)$$

$$Ro w(z_1) = \lambda[\varepsilon\partial_t \eta + Ro(u\partial_x \eta + v\partial_y \eta)], \quad (7)$$

$$\pi(x, y, z_1, t) = \frac{\lambda Bu}{Ro}\eta(x, y, t) \quad (8)$$

where  $\eta(x, y, t)$  is the dimensionless deviation of the free-surface.

We have introduced in this formulation the following non-dimensional parameters:

- The *Ekman number*  $E_k = \frac{\nu}{fH^2}$  fix the vertical scale  $\delta_E = \sqrt{E_k}H_0 = \sqrt{\nu/f}$  of the viscous Ekman layer, where  $\nu$  is the fluid viscosity. According to the standard boundary layer theory, this viscous layer cannot be neglected at the bottom boundary where the no-slip condition (6) must be satisfied (Gill, 1982; Pedlosky, 1987; Vallis, 2006). In the laboratory, the thickness of this boundary layer is fixed only by the rotation rate  $\Omega_0 = 2\pi/T_0$ . For typical values of  $\Omega_0 \simeq 1-10$  rpm we get  $\delta_E \simeq 1-2$  mm. Hence, as far as  $H_0 \gg \delta_E$ , we usually neglect viscous effects in the upper part of the fluid layer ( $z \geq 2 - 3\delta_E$ ). Nevertheless, the Ekman layer forces a secondary re-circulation which induces an efficient transfer of angular momentum from the boundary to the whole fluid domain (Greenspan, 1968). For a fluid layer close to the geostrophic balance the characteristic decay time of this Ekman pumping is  $T_E = H_0/\sqrt{\nu f} = T_0/(4\pi\sqrt{E_k})$  (Pedlosky, 1987). Therefore, if we want to neglect this dissipative process over at least several rotation period  $T_0$ , the Ekman number should be quite small  $E_k \leq 10^{-4}$ . Such values can be easily reached if the fluid layer is thick enough.
- The *aspect ratio parameter*  $\alpha = H_0/L$ . While this parameter is generally small for synoptic atmospheric or oceanic structures ( $\alpha \simeq 10^{-2}-10^{-3}$ ), this is not always the case in laboratory experiments. Indeed, we could hardly work with

1 ultra-thin layers. The first limitation is due to the surface tension which acts 1  
 2 on a millimeter scale. The second constraint is due to the Ekman pumping 2  
 3 described above. Hence, typical layer depths in rotating tank experiments are 3  
 4 about few tens of centimeters  $H_0 \simeq 10\text{--}50$  cm. Therefore, in order to get a 4  
 5 small aspect ratio (at least  $\alpha \simeq 0.1$ ) the characteristic horizontal scales should 5  
 6 be about  $L \simeq 1\text{--}5$  m. To study the dynamics of multiple structures or to avoid 6  
 7 the end effects, the experiment should then be done on a very large turntable 7  
 8  $D \simeq 10$  m. A unique installation reaches such large scale ( $D = 13$  m), the 8  
 9 Coriolis turntable<sup>1</sup> in Grenoble, France. However, for medium size experiments 9  
 10 ( $D \simeq 1\text{--}2$  m) the aspect ratio parameter cannot be asymptotically small and is 10  
 11 often close to unity  $\alpha \simeq 1$ . 11

- 12 • The classical *Rossby number*  $Ro = \frac{U}{fL}$  characterizes the importance of rota- 12  
 13 tion in the fluid layer. In order to be consistent, the horizontal scale  $L$  in the 13  
 14 Rossby number  $Ro$  should correspond to the characteristic scale of the hori- 14  
 15 zontal velocity gradient. In other words, the Rossby number quantifies the ratio 15  
 16 of the relative vorticity  $\zeta = \partial_x v - \partial_y u$  with respect to the planetary vorticity 16  
 17 ( $Ro \simeq \zeta/f$ ). For large-scale flows, the Rossby number is generally small or fi- 17  
 18 nite in the atmosphere and the ocean, leading to the geostrophic balance. It will 18  
 19 exceed unity only for very intense vortices, such as hurricanes. This parameter 19  
 20 is usually well controlled in a rotating experiment and both small and large val- 20  
 21 ues could be obtained. Nevertheless, to reach large value which would exceed 21  
 22 unity an external forcing is generally needed. Indeed, without external energy 22  
 23 source, from any initial state the geostrophic adjustment process will quickly 23  
 24 lead to a mean flow in geostrophic balance which implies small or finite Rossby 24  
 25 numbers ( $Ro \leq 1$ ). 25
- 26 • We introduce here the *time evolution parameter*  $\varepsilon = \frac{1}{fT}$ . This parameter 26  
 27 quantifies the dynamical evolution of the flow. It depends on the flow re- 27  
 28 sponse to the initial condition or to the external forcing. Hence, this parameter 28  
 29 cannot be fixed by the experimental setup. Classical textbooks (Gill, 1982; 29  
 30 Pedlosky, 1987) usually consider the case of large-scale and slow advective 30  
 31 motion and therefore the time-evolution parameter and the Rossby number are 31  
 32 fixed to be of the same order  $\varepsilon \simeq Ro$ . However, for high frequency linear waves 32  
 33 (i.e. short gravity-waves)  $\varepsilon \geq 1$  and  $Ro \ll 1$  while for intense cyclones  $Ro \geq 1$  33  
 34 and  $\varepsilon \ll 1$ . Hence, as far as experiments on geostrophic adjustment are con- 34  
 35 cerned, it is useful to consider both the cases of slow ( $\varepsilon \ll 1$ ) advective motion 35  
 36 or fast ( $\varepsilon \geq 1$ ) wave motion independently of the Rossby number value. 36
- 37 • The *Burger number*  $Bu = (R_d/L)^2$  where  $R_d = \sqrt{gH_0}/f$  is the Rossby deforma- 37  
 38 tion radius. As far as we consider a relatively thick layer  $H_0 \simeq 10\text{--}50$  cm 38  
 39 and a relatively slow rotation rate  $\Omega_0 \simeq 1\text{--}10$  rpm we get a large deforma- 39  
 40 tion radius  $R_d \geq 50$  cm which is usually close to the size of the experi- 40  
 41 mental apparatus. Hence, with a single barotropic layer, we can hardly obtain 41

42 <sup>1</sup> <http://www.coriolis-legi.org>.

small Burger number values. Only few experiments using high rotation speed ( $\Omega_0 \simeq 60$  rpm) reached small Burger number value within a single layer configuration. However, in such case a parabolic vessel is needed to compensate the resulting parabolic shape of the free-surface (Nezlin and Snezhkin, 1993; Stegner and Zeitlin, 1998; van de Konijnenberg, Nielsen, Rasmussen and Stenum, 1999). For such setups the strong curvature of the fluid layer induces, as in the spherical planetary geometry, a strong beta effect. Hence, such parabolic configurations are relevant to model large-scale planetary flows, as the Jovian atmosphere for instance.

- The *relative elevation parameter*  $\lambda = \eta_0/H_0$  where  $\eta_0$  is the characteristic amplitude of the free surface deviation. When the flow is close to geostrophic balance, namely when the dynamical pressure gradient  $\nabla\pi$  is balanced at the same order by the Coriolis force, the relative geopotential deviation  $\lambda$  depends on both the Rossby and the Burger number  $\lambda \sim Ro/Bu$  (cf. Chapters 1 and 2).

The RSW model is based on three main approximations: weak dissipation, hydrostatic balance and quasi-bidimensionality of the horizontal velocity. We discuss, in what follows, when and in which range of dynamical parameters these approximations could be valid or not.

We first assume the *hydrostatic balance* for the whole pressure field. The vertical acceleration in (3) could be neglected if both  $\alpha^2 Ro \ll 1$  and  $\alpha^2 \varepsilon \ll 1$ . Note that for rotating flows, the shallow-water constraint ( $\alpha \ll 1$ ) is not necessary to get the hydrostatic balance. Indeed, a weakly viscous ( $E_k \ll 1$ ) slow ( $\varepsilon \ll 1$ ) and geostrophic ( $Ro \ll 1$ ) flow will follow the hydrostatic balance even if the aspect ratio parameter  $\alpha$  is finite. Hence, hopefully for the experimentalists, quasi-geostrophic motions can be accurately reproduced in a rotating tank while  $\alpha \simeq 1$ . Nevertheless, the shallow-water constraint is not a sufficient condition that guarantees the hydrostatic balance. Indeed, if the system supports high frequency waves ( $\varepsilon \gg 1$ ) they could be a source of non-hydrostatic motion or instability. Besides, the case of intense ( $Ro \simeq 1$ ) shallow-water ( $\alpha \ll 1$ ) vortices or jets is also complex. These intense structures could exhibit in anticyclonic vorticity region an inertial or centrifugal instability which generate three-dimensional and non-hydrostatic perturbations within the large scale flow (Teinturier, Stegner, Viboud, Didelle and Ghil, 2006). Such short-wavelength instabilities could amplify small-scale perturbations (having a finite aspect ratio  $\alpha_p \simeq 1$ ) with a rapid growth rate ( $\varepsilon_p \simeq 1$ ). In such case, the cyclonic vorticity regions may satisfy the hydrostatic balance, while intense non-hydrostatic motion occurs in the anticyclonic regions (cf. Figure 5 below).

However, when the evolution of a shallow-water flow (or its unstable perturbations) is not fast ( $\varepsilon \leq 1$ ) the hydrostatic balance is satisfied at the first order of approximation and equation (3) leads to:

$$\partial_z \pi = 0. \tag{9}$$

Then according to (8) the dynamical pressure becomes directly proportional to the free-surface geopotential deviation:

$$\pi(x, y, t) = \eta(x, y, t). \quad (10)$$

We then assume that the fluid layer experiences a *weak dissipation*. The viscous terms in equations (1)–(2) could be neglected at a first order of approximation if the Ekman number is small enough  $E_k \ll 1$ . However, we cannot totally suppress the no-slip condition at the bottom and we should introduce an Ekman layer. This layer will then change the bottom boundary conditions for the upper inviscid layer. It will allow a free-slip condition for the horizontal velocities ( $u(z_0)$ ,  $v(z_0)$ ) but will induce a non-zero vertical velocity. In the case of hydrostatic and slow geostrophic motions this vertical velocity is proportional to the horizontal flow vorticity (Pedlosky, 1987; Vallis, 2006) and the boundary conditions (6) should be replaced by:

$$w(z_0) = \sqrt{\frac{E_k}{2}} (\partial_x v - \partial_y u) = \sqrt{\frac{E_k}{2}} \zeta \quad (11)$$

where  $\zeta$  is the vertical component of vorticity. Hence, the horizontal dissipation and the Ekman pumping mechanism could be neglected if  $\sqrt{E_k} \ll 1$ . Practically, in laboratory experiments the dissipation will be a second order process when  $E_k \leq 10^{-4}$  at least.

The third approximation assume a *quasi-bidimensional horizontal flow*, in other words, the vertical derivatives  $\partial_z u$  and  $\partial_z v$  are expected to be negligible. This assumption corresponds to the Taylor–Proudman theorem which is valid only in the limit of small Rossby number (geostrophic flows). A similar approximation is made by the closure hypothesis (22) given in the introduction, which decorrelate the vertical averaging of the horizontal velocity field. Then integrating the continuity equation (22) along the vertical and using the boundary conditions (7) and (11) we finally obtain the following dimensionless formulation of the RSW model:

$$\varepsilon \partial_t u + Ro \mathcal{D}_h u - v = -\partial_x \eta, \quad (12)$$

$$\varepsilon \partial_t v + Ro \mathcal{D}_h v + u = -\partial_y \eta, \quad (13)$$

$$\lambda [\varepsilon \partial_t \eta + Ro \mathcal{D}_h \eta] + (1 + \lambda \eta) Ro [\partial_x u + \partial_y v] = Ro \sqrt{\frac{E_k}{2}} \zeta \quad (14)$$

where  $\mathcal{D}_h = u \partial_x + v \partial_y$  and  $\zeta = \partial_x v - \partial_y u$ .

Strictly speaking, these RSW equations are valid in the asymptotic limit of slow quasi-geostrophic flows even if the aspect ratio parameter is finite  $\alpha \simeq 1$ . However, this model is often accurate beyond its limit of validity for finite Rossby number ( $E_k \ll 1$ ;  $\varepsilon \ll 1$ ;  $Ro \leq 1$ ) and could be applied to a wide variety of laboratory experiments. This will be indeed the case if the vertical motions remain

1 weak enough ( $w \ll 1$ ). This latter condition implies both the hydrostatic balance  
 2 (9) and a quasi-bidimensional horizontal flow. Nevertheless, in such case, high-  
 3 order terms should be added in (11) to account for non-linear Ekman pumping  
 4 (Zavala Sanson and van Heijst, 2000; Hart, 2000).

6 1.2. Influences of the centrifugal force

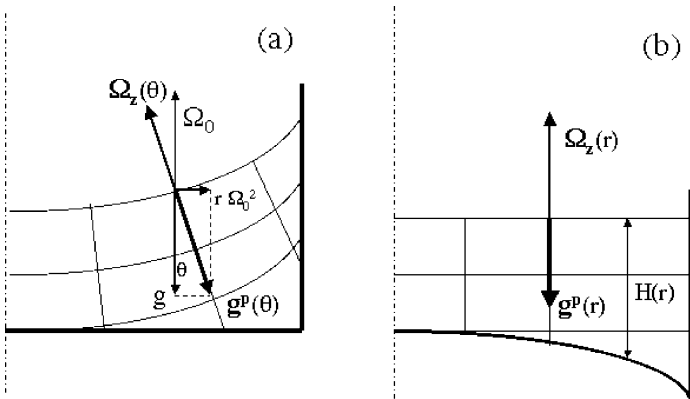
8 Since the Newton's bucket experiment (1689) it is well known that the free-  
 9 surface of a fluid layer in solid body rotation is deformed under the action of  
 10 the centrifugal force. The surfaces of constant pressure for a fluid at rest in the  
 11 rotating frame (i.e. equipotential surfaces  $\Phi = cst$ ) are given by the potential  
 12 function:

$$13 \quad \Phi(R, Z) = -\frac{1}{2}\Omega_0^2 R^2 + gZ. \quad (15)$$

15 Hence, the free-surface of a rotating fluid layer satisfies a parabolic shape. More-  
 16 over, according to (15), all the equipotential surfaces corresponds to the same  
 17 paraboloid simply translated along the rotation axis (Figure 2(a)). We use in what  
 18 follows a dimensionless formulation where  $H_0$  is the mean thickness of the layer,  
 19  $D$  is the tank diameter and  $Z_c = g/\Omega_0^2$  is the curvature radius at the center of the  
 20 parabola. In cylindrical coordinates, the equation for the unperturbed free-surface  
 21 can be written as:

$$22 \quad h(r) = \frac{Z}{H_0} = 1 + \frac{1}{2H_0Z_c} \left( R^2 - \frac{1}{8}D^2 \right) = 1 + \frac{1}{2} \frac{\beta}{\alpha} \left( r^2 - \frac{1}{8}d^2 \right). \quad (16)$$

25 We have introduced here two dimensionless parameters:



40 Figure 2. Parabolic deformation of the equipotential surfaces (thin lines) due to the centrifugal  
 41 acceleration in rotating laboratory experiments (a). Schematic description of the tangent plane ap-  
 42 proximation when the corrective terms of order  $\beta^2 d$  could be neglected (b).

- 1 • The *dimensionless tank diameter*  $d = D/L$ . The experimentalist tend to use a  
2 large tank  $d \gg 1$  in order to satisfy the shallow-water constraint and to avoid  
3 the boundary effects. However, for such case, the influence of the centrifugal  
4 force could become non negligible close to the wall.
- 5 • The *curvature parameter*  $\beta = L/Z_c$  quantifies the influence of the curved  
6 equipotential surfaces on a dynamical structure of horizontal size  $L$ . For the  
7 atmosphere or the oceans an equivalent parameter is induced by the spheri-  
8 cal geopotential where  $Z_c$  is replaced by the earth radius  $R_E$ . It is there-  
9 fore natural to chose a coordinate system so that the unperturbed water sur-  
10 face, or any equipotential surfaces, is given by  $z = cst$ . Hence, paraboloidal  
11 coordinates should be used for rotating laboratory experiments (Nycander,  
12 1993) while spherical coordinates are used for planetary flows (Pedlosky,  
13 1987). However, for small values of the curvature parameter ( $\beta \ll 1$ ) the  
14 tangent plane approximation is generally made. In other words, a Cartesian  
15 system of coordinates is used locally and the corrective terms induced by  
16 the parabolic curvature will appear only at the order  $\beta^2 d$  (Nycander, 1993;  
17 Stegner and Zeitlin, 1998). If we consider a medium scale experiment ( $D \simeq$   
18 100 cm) and a typical horizontal scale  $L \simeq 10$  cm, these corrective terms could  
19 be neglected for moderate rotation rate ( $\Omega_0 \leq 10$  rpm).

20 The main difference between rotating laboratory experiments and planetary flows  
21 is that the effective gravity  $g^e$  is variable in both direction and amplitude in the  
22 laboratory. Indeed, when the centrifugal force is not negligible, it induces a tilting  
23 of the effective gravity but also a change in its amplitude (Figure 2(a)). The latitudi-  
24 nal dependence of the effective gravity (also called the  $\gamma$ -effect) in paraboloidal  
25 coordinates and in the tangent plane approximation is given by:

$$26 \frac{g^e}{g} = \frac{1}{\cos \theta} = \sqrt{1 + \beta^2 r^2} \simeq 1 + \frac{1}{2} \beta^2 r^2. \quad (17)$$

27 For paraboloidal equipotential surfaces this latitudinal dependence of the ef-  
28 fective gravity is of the same order than the latitudinal dependence of the Coriolis  
29 force (classical  $\beta$ -effect).

$$30 \frac{f}{f_0} = \frac{\Omega_z}{\Omega_0} = \cos \theta \simeq 1 - \frac{1}{2} \beta^2 r^2. \quad (18)$$

31 Under the tangent plane approximation the equipotential surface are assumed  
32 to be locally flat (Figure 2(b)) while the radial variations of the effective gravity  
33  $g^e$ , the local component of rotation  $\Omega_z$  and the unperturbed layer depth  $h$  are  
34 expanded at the first order in  $y = r - a$  the local latitudinal coordinate centered  
35 at the radial position  $r \simeq a$ .

36 If we consider the center of the rotating tank ( $a = 0$  and  $y = r$ ), according  
37 to (16)–(18) the latitudinal variations of  $h(y)$ ,  $\Omega_z(y)$  or  $g^e(y)$  are all quadratic  
38  
39  
40  
41  
42

and when  $\beta/\alpha = L^2/(Z_c H_0) \ll 1$  the fluid layer respect the  $f$ -plane configuration at the first order of approximation. This will be generally the case for moderate rotation rate ( $\Omega_0 \leq 10$  rpm) in a central region of few tens of centimeter ( $r \leq 10$ – $20$  cm). However, out from the center, the latitudinal variations could be linearly expended in  $y$  and they reach their extremal values at the tank wall. Therefore, in order to quantify the relative influence of the  $\beta$ -effect, the  $\gamma$ -effect or the topography, we estimate (when  $a = d$ ) the magnitude of the following first derivatives:  $\partial_y h/h \propto \beta d/\alpha$ ,  $\partial_y f/f \propto \beta^2 d$  and  $\partial_y g^e/g^e \propto \beta^2 d$ . Hence, for standard experimental configuration ( $\beta \ll 1$ ,  $\alpha \leq 1$ ,  $d \gg 1$ ) the  $y$ -dependence of the equilibrium layer depth induces by the parabolic free-surface deformation is the dominant effect. Due to this topographic effect, the equilibrium fluid layer can support topographic-Rossby waves. The linear dispersion relation of these low-frequency waves is analogous to planetary Rossby waves and they are strongly coupled with the slow geostrophic motion. This effect may induces, for instance, a significant drift velocity ( $V_d \simeq fL(\partial_y h/h)$  when  $L \leq R_d$ ) and the dispersion of localized vortices (Masuda, Marubayashi and Ishibashi, 1990; Carnevale, Kloosterziel and van Heijst, 1991; Flor and Eames, 2002). Hence, the dynamical influence of the topographic variations could be neglected in the whole tank, from the center to the wall, if  $\partial_y h/h \propto \beta d/\alpha \ll \varepsilon$ . The latter criterion will be generally satisfied in a medium scale experiment ( $D \simeq 100$  cm) if the rotation rate is weak enough ( $\Omega_0 \leq 4$  rpm).

However, if the ratio  $\beta d/\alpha$  become too large, the variation of the layer thickness induced by the centrifugal force could be compensated with a parabolic bottom topography or a parabolic vessel adjusted to the rotation rate (Nezlin and Snezhkin, 1993; Stegner and Zeitlin, 1998; van de Konijnenberg, Nielsen, Rasmussen and Stenum, 1999).

### 1.3. Non-hydrostatic wave modes

Focusing on the geostrophic adjustment problem, where both slow geostrophic motion and fast waves are generated, we look here more carefully at the wave motion that may occurs in a rotating fluid layer. We linearize the primitives equations (1)–(8) assuming small amplitudes for the velocity  $Ro \ll 1$  and the free surface displacement  $\lambda \ll 1$ . We neglect all dissipative terms ( $E_k \ll 1$ ) and take the deformation radius as a characteristic horizontal scale  $L = R_d$  of the unperturbed rotating fluid layer, therefore  $Bu = 1$  and  $\alpha = H_0/R_d$ . Besides, we keep in mind that the aspect ratio  $\alpha$  cannot be asymptotically small for laboratory experiment and we keep the vertical acceleration in (3). Hence, we get:

$$\varepsilon \partial_t u - v = -\partial_x \pi, \quad (19)$$

$$\varepsilon \partial_t v + u = -\partial_y \pi, \quad (20)$$

$$\alpha^2 \varepsilon \partial_t w = -\partial_z \pi, \quad (21)$$

$$\partial_x u + \partial_y v + \partial_z w = 0 \quad (22)$$

with upper ( $z_1 = 1$ ) and lower ( $z_0 = 0$ ) boundary conditions

$$w(z_0) = 0, \quad (23)$$

$$w(z_1) = \varepsilon \partial_t \eta, \quad (24)$$

$$\pi(z_1) = \eta. \quad (25)$$

According to the space and time shift invariance of the system, we use the following Fourier decomposition  $A(x, y, z, t) = A_0(z)e^{i(t-kx-ly)}$  for all variables. In this case the temporal evolution parameter corresponds to a dimensionless wave frequency  $\varepsilon = \tilde{\omega}/f$ . This linear system finally leads to:

$$\partial_z^2 \pi_0 + \frac{\alpha^2 \varepsilon^2 K^2}{1 - \varepsilon^2} \pi_0 = 0 \quad (26)$$

where  $K^2 = k^2 + l^2$ , with the boundary conditions

$$\partial_z \pi_0(0) = 0, \quad (27)$$

$$\partial_z \pi_0(1) = \alpha^2 \varepsilon^2 \pi_0(1). \quad (28)$$

For *inertia-gravity waves* ( $\varepsilon > 1$ ) we obtain the following dispersion relation:

$$\gamma \tanh(\gamma) = \alpha^2 \varepsilon^2; \quad \gamma^2 = \frac{\alpha^2 \varepsilon^2 K^2}{\varepsilon^2 - 1}. \quad (29)$$

We can see here that we will recover the dispersion relation of Poincaré waves

$$\varepsilon^2 = 1 + K^2 \quad (30)$$

only if  $\alpha K \ll 1$ , in such case short inertia-gravity waves are dispersionless. This condition is more restrictive than the shallow-water constraint  $\alpha \ll 1$ , and indeed short enough gravity waves will always deviate from the RSW model. We have plotted in [Figure 3](#) the deviation from the Poincaré dispersion relation for various values of the aspect ratio parameter  $\alpha$  that could be found in laboratory experiment.

For a finite value of the aspect ratio parameter,  $\alpha = 0.3$  for instance as it is shown in [Figure 4](#), high-frequency waves ( $\varepsilon \gg 1$ ) or in other words short-waves ( $K \gg 1$ ) will satisfy the dispersion relation of non-rotating surface gravity waves (SGW).

$$\varepsilon^2 = \frac{K}{\alpha} \tanh(\alpha K). \quad (31)$$

It can be shown that the same dispersion relation (31) applies for boundary Kelvin waves propagating along a lateral wall of the tank. Hence, unlike the RSW model,

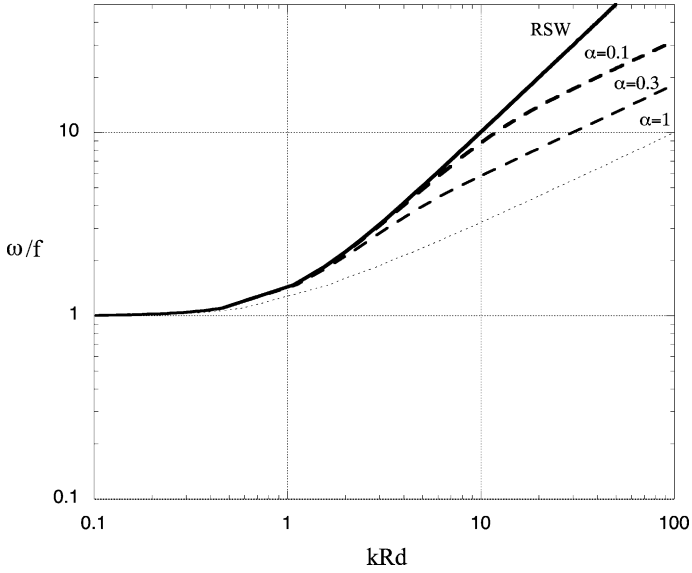


Figure 3. Log–log plot of the dimensionless dispersion relation for inertia–gravity waves. The curves correspond to different values of the aspect ratio parameter: RSW model, or  $\alpha = 0$  (thick line),  $\alpha = 0.1$  (thick dashed line),  $\alpha = 0.3$  (thin dashed line),  $\alpha = 1$  (thin dotted line).

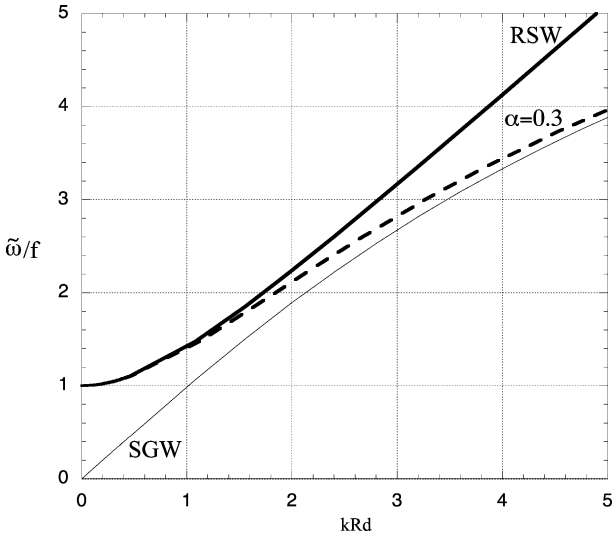


Figure 4. Dimensionless dispersion relation of inertia–gravity waves corresponding to the RSW model (thick line), in a non-rotating (thin line) and a rotating fluid layer (thick dashed line) for the fixed value of  $\alpha = H_0/R_d = 0.3$ .

both inertia–gravity waves and Kelvin waves will become dispersive in the short-wave limit if the aspect ratio parameter is not small enough. Nevertheless, these non-hydrostatic effects could be neglected for a wide range of the inertia–gravity wave spectrum if  $\alpha K \ll 1$ , which corresponds to

$$\tilde{\lambda} \gg 2\pi H_0 \quad (32)$$

where  $\tilde{\lambda}$  is the characteristic wavelength.

For *inertial waves* ( $\varepsilon < 1$ ) we obtain a discrete spectrum of  $n$  vertical modes which correspond to the dispersion relations:

$$-\gamma_n \tan(\gamma_n) = \alpha^2 \varepsilon_n^2; \quad \gamma_n^2 = \frac{\alpha^2 \varepsilon_n^2 K_n^2}{1 - \varepsilon_n^2} \quad (33)$$

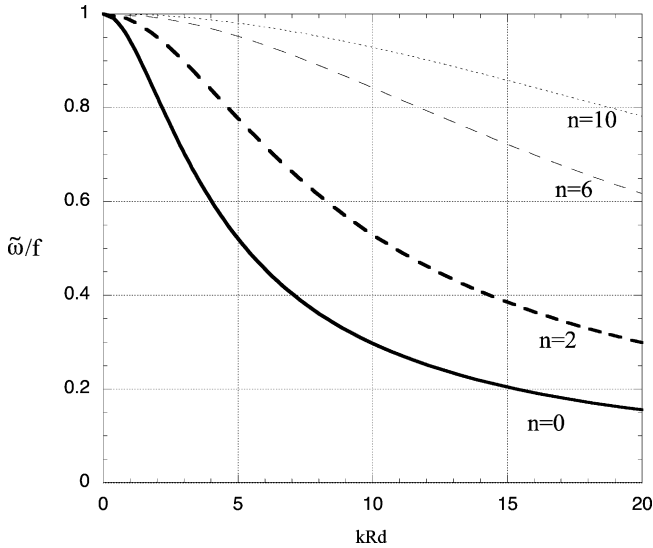
where  $(1 + n)\pi/2 < \gamma_n < (1 + n)\pi$ .

These non-hydrostatic waves exhibit strong variations of pressure and velocity along the vertical axis (Figure 5(b)). When the vertical wavenumber becomes large ( $n \gg 1$ ) the wave frequency approaches the Coriolis frequency  $\varepsilon \simeq 1$  for a wide range of horizontal wavenumber components. According to Figure 5(a), for a given horizontal wavelength  $k$ , the short wavelength perturbations along the vertical will have the highest horizontal phase speed. Hence, the non-hydrostatic inertial waves play a crucial role in the vertical alignment and the rapid formation of Taylor columns in a rotating fluid layer.

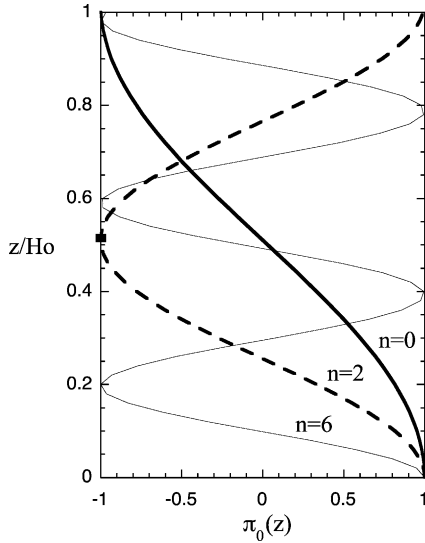
If now we add a mean flow component, such type of non-hydrostatic modes will lead to inertial instability in anticyclonic vorticity regions (Johnson, 1963; Yanase, Flores, Metais and Riley, 1993). Such instabilities occur when the Rossby number  $Ro$  exceeds unity and the maximum growth rates for these three-dimensional modes are reached when  $Ro \simeq 2$ . For larger Rossby numbers, the influence of rotation becomes negligible, and the growth rates of such unstable modes are strongly reduced. Hence, for finite Rossby numbers, starting initially from a two-dimensional flow the three-dimensional perturbations could grow exponentially and break both the hydrostatic and the geostrophic balance (Afanasyev and Peltier, 1998; Stegner, Pichon and Beunier, 2005). As it can be seen in Figure 6, such small-scale instability may occur in shallow-water anticyclonic vortices when the Rossby number is large enough.

#### 1.4. Two-layer stratification

We have seen previously that with a single barotropic layer experiment the deformation radius is generally close to the tank size. In other words, for a single layer  $f$ -plane experiment we are restricted to large Burger number dynamics. Nevertheless, if we use a two-layer stratification we introduce a baroclinic deformation



(a)



(b)

Figure 5. Dimensionless dispersion relation of non-hydrostatic inertial waves (a) corresponding to various vertical modes (b). All these wave modes are calculated for the aspect ratio parameter  $\alpha = H_0/R_d = 1$ .



Figure 6. Dye visualisation of von Karman wake in a rotating shallow-water layer with  $\alpha \simeq 0.07$ ,  $Ro \simeq 2$  and  $Re \simeq 20000$ . Small-scale instability is visible in anticyclonic vortices (black dye), while cyclonic vortices (red dye) remain stable (Teinturier, Stegner, Viboud, Didelle and Ghil, 2006).

radius which could be much smaller than the barotropic one. Besides, the Ekman pumping affects only the lower layer, and for an appropriate set of parameters the upper layer dissipation could be strongly reduced.

To create a density stratification in water, salt or sugar are generally used instead of temperature. Indeed, the thermal diffusivity ( $\kappa_T \simeq 10^{-7} \text{ m}^2 \text{ s}^{-1}$ ) is a hundred time larger than the salt diffusivity ( $\kappa_S \simeq 10^{-9} \text{ m}^2 \text{ s}^{-1}$ ). In a motionless fluid layer, an initial salt perturbation will diffuse over a 1 cm distance in half a day instead of ten minutes for a thermal perturbation. Hence, for typical layers depth about few to tens of centimeters an initial salt or sugar stratification will remain robust for at least several hours. To obtain a sharp density jump corresponding to a well-defined two-layer stratification we generally proceed as follows. The tank is first filled with the deep and dense lower layer. Then, we start to spin up the rotating table and when the solid-rotation is reached we slowly inject the light upper layer  $\rho_1$  at the surface of the dense bottom layer  $\rho_2$ . To reduce the vertical

1 mixing during the injection we could use floating Hele-shaw cells or small tubes  
 2 to inject the light fluid horizontally at the free-surface. An other method consists  
 3 to inject very slowly the upper layer through floating porous plates.

4 Let us consider a two-layer salt stratification, as shown in figure. According to  
 5 the classical dimensional analysis we add to the previous ones at least four new  
 6 dimensionless parameters:

- 7 • The *thickness ratio parameter*  $\delta = H_1/(H_1 + H_2)$ . This parameter controls  
 8 the dynamical interaction between the two layers. For equivalent depth layers  
 9  $\delta \simeq 0.5$  the two layers are strongly coupled and baroclinic instability  
 10 may occurs even if the vertical velocity shear is weak. On the other hand, according  
 11 to the standard two-layer Phillips model (Pedlosky, 1987), for small  
 12 ratios  $\delta \ll 1$ , the baroclinic growth rates tend to vanish. Hence, to avoid a  
 13 strong baroclinic destabilisation of the flow, we will first consider laboratory  
 14 experiments with a thin upper layer and a deep lower layer having  $\delta \simeq 0.1$ .  
 15 Besides, in order to keep the Ekman number small enough in the lower layer  
 16 ( $E_k^{(2)} = (\delta_E/H_2)^2 \leq 10^{-4} E_k$ ), we generally fix  $H_2 = 10\text{--}20$  cm, and therefore  
 17 the upper layer thickness is about  $H_1 \simeq 2$  cm.
- 18 • The *density ratio parameter*  $N = 2(\rho_2 - \rho_1)/(\rho_2 + \rho_1)$ . With salt stratification,  
 19 we can easily obtain a  $N$  small up to  $10^{-3}$ . We then introduce the reduced  
 20 gravity  $g' = Ng \ll g$  which controls the dynamics of internal gravity waves at  
 21 interface between the layers.
- 22 • The *internal Burger number*  $Bu' = (R'_d/L)^2$  corresponding to the baroclinic  
 23 deformation radius  $R'_d = \sqrt{g'H_1H_2(H_1 + H_2)}/f$ . We can see here that for  
 24 small  $N \simeq 10^{-3}$  and  $\delta \simeq 0.1$  the baroclinic deformation radius could be  
 25 two orders of magnitude smaller than the barotropic deformation radius  $R'_d \simeq$   
 26  $\sqrt{g'H_1}/f \simeq 10^{-2} R_d$ , where  $R_d = \sqrt{g(H_1 + H_2)}/f$ . Hence, for a thin upper  
 27 layer with  $H_1 \simeq 2$  cm and a weak density difference  $\rho_2 - \rho_1 \simeq 2\text{--}10$  g l<sup>-1</sup>  
 28 we can reach deformation radius as small as  $R'_d \simeq 1$  cm. Therefore, with a  
 29 two-layer stratification, the internal Burger number could be easily varied from  
 30 small to large values  $0.01 \leq Bu' \leq 100$ .
- 31 • We introduce the *stratification parameter*  $E_S = (\delta_E/d_S)^2$  in order to quantify  
 32 the dissipation induced by the fluid–fluid interface. This parameter is an  
 33 equivalent Ekman number for a continuously stratified fluid where  $d_S$  is the  
 34 characteristic scale of the vertical density gradient. Indeed, for salt stratification,  
 35 due to the molecular diffusion and the injection process, the density  
 36 gradient is always continuous between the upper and the lower layer. Even  
 37 with very slow laminar injection of both layers the characteristic size  $d_S$  cannot  
 38 be infinitely small, and we generally get a density gradient thickness of  
 39  $d_S = 3\text{--}5$  mm (Stegner, Bouruet-Aubertot and Pichon, 2004). For geostrophic  
 40 flows, the vertical gradient of the horizontal velocity will be directly proportional  
 41 to the vertical density gradient. Hence, the dissipative terms in the  
 42

right-hand side of the horizontal momentum equations (12) should scale with  $E_S = (\delta_E/d_S)^2$ . This parameter is larger than the Ekman number defined using the upper layer thickness  $E_k^{(1)} = (\delta_E/H_1)^2$ . However, due to the absence of the no-slip boundary condition, there is no boundary Ekman layer for the upper layer. The fluid–fluid interface will then induce (if any) a much weaker recirculation than a classical bottom Ekman layer if the vertical stratification is not too sharp  $E_S = (\delta_E/d_S)^2 \ll 1$ .

We get a dimensionless set of equation for the two-layer RSW model with rigid lid and bottom boundary condition using:  $L$  as horizontal scale and  $T$  the characteristic time-scale for both layers,  $U^{(i)}$  as the horizontal velocity,  $H_i$  the vertical thickness and  $\rho_i f U^{(i)} L$  the pressure deviation from hydrostatic balance in each layer.

$$\varepsilon \partial_t u^{(i)} + Ro^{(i)} \mathcal{D}_h^{(i)} u^{(i)} - v^{(i)} = -\partial_x \pi^{(i)}, \quad (34)$$

$$\varepsilon \partial_t v^{(i)} + Ro^{(i)} \mathcal{D}_h^{(i)} v^{(i)} + u^{(i)} = -\partial_y \pi^{(i)} \quad (35)$$

where  $\mathcal{D}_h^{(i)} = u^{(i)} \partial_x + v^{(i)} \partial_y$  and the superscript  $i = 1, 2$  corresponds respectively to the upper and the lower layer. The pressure continuity at the interface gives:

$$\frac{\lambda B u'}{1 - \delta} \eta = (1 - N) Ro^{(1)} \pi^{(1)} - (1 + N) Ro^{(2)} \pi^{(2)} \quad (36)$$

and the mass conservation in each layer leads to:

$$\lambda [\varepsilon \partial_t \eta + Ro^{(1)} \mathcal{D}_h^{(1)} \eta] + (1 + \lambda \eta) Ro^{(1)} [\partial_x u^{(1)} + \partial_y v^{(1)}] = 0, \quad (37)$$

$$\begin{aligned} & \lambda \delta [\varepsilon \partial_t \eta + Ro^{(2)} \mathcal{D}_h^{(2)} \eta] - (1 - \delta - \lambda \delta \eta) Ro^{(2)} [\partial_x u^{(2)} + \partial_y v^{(2)}] \\ & = (1 - \delta) Ro^{(2)} \sqrt{\frac{E_k^{(2)}}{2}} \zeta^{(2)} \end{aligned} \quad (38)$$

where the relative elevation parameter  $\lambda$  corresponds here to the characteristic deviation of the internal interface rescaled by the upper layer thickness  $H_1$ .

According to the above equations, if the thickness ratio parameter  $\delta$  and the density ratio parameter  $N$  are small enough and if the motion has a strong baroclinic component (intense velocities in the thin upper layer while the deep lower layer remains almost at rest  $Ro^{(2)} \simeq \delta Ro^{(1)}$  (Cushman-Roisin, Sutyryn and Tang, 1992), the interface deviation  $\eta$  is controlled by the upper layer pressure only  $\eta \simeq \pi^{(1)}$ . In such case, at the first order of approximation, the upper layer motion is not affected by the lower layer which acts as a neutral layer. Hence, the upper layer dynamics can be described by the shallow-water reduced-gravity model. Namely, a one layer RSW model where the gravity  $g$  is replaced by the reduced gravity  $g'$  induced by the two-layer stratification.

Table 1

	Vortical motion	Wave motion
Single layer	$\varepsilon\alpha^2 \ll 1; Ro\alpha^2 \ll 1; Ro < 1$	$kH_0 \ll 1$
Two layers	$\delta \ll 1; Ro^{(2)} \leq \delta Ro^{(1)}; Ro^{(i)}(\alpha^{(i)})^2 \ll 1; Ro^{(1)} < 1$	$kH_2 \ll 1$

However, as for the single layer case, non-hydrostatic wave motions or inertial instability may occur in the two-layer experiment when respectively  $\tilde{\lambda} \gg 2\pi H_2$  or  $Ro^{(1)} > 1$ . Note that the hydrostatic constraint on the wave activity is fixed here by the deep layer thickness  $H_2$  and not the thin upper layer  $H_1$ . Recent laboratory experiments performed in a two-layer configuration ( $\alpha \simeq 0.66$ ;  $\delta \simeq 0.2$ ) exhibit non-hydrostatic wave behaviour for  $\tilde{\lambda} \simeq 80$  cm wavelength, while  $H_1 \simeq 12.5$  cm and  $H_2 \simeq 50$  cm (Thivolle-Cazat, 2003).

Taking into account the above mentioned laboratory constraints, the physical modelling of rotating shallow-water flows looks like a Holy Grail for experimentalist. Nevertheless, for a specific range of the dynamical parameters, the motion in rotating fluid layers could be close to the one layer RSW model. We recall below, both for single-layer and the two-layer configurations, the distinct conditions needed to be satisfied, respectively, for the slow vortical motion and the fast wave motion in order to follow the RSW dynamics. See Table 1.

## 2. Potential vorticity measurements: a new challenge

Both vorticity and potential vorticity play an important role in the dynamics of rotating fluid layers. The application of the Kelvin theorem to a non-dissipative rotating shallow-water flow implies the Lagrangian conservation of potential vorticity (Chapter 3) in each layer.:

$$\frac{D}{Dt} \left( \frac{1 + Ro\zeta}{1 + \lambda\eta} \right) = 0. \quad (39)$$

An elementary fluid parcel (i.e. fluid column) moving within a layer could be stretched or compressed. These changes in the height of the fluid parcel during its motion will be accompanied by a change in its vorticity. In other words, for a purely incompressible two-dimensional flow when the free-surface or the interface deviations are negligible ( $\lambda \ll Ro$ ), we recover the Lagrangian conservation of vorticity:

$$\frac{D\zeta}{Dt} = 0. \quad (40)$$

In this case, vorticity will be generated in the flow only if there is an external source (boundary layer or fluid injection, for instance). For a rotating fluid layer,

1 if the layer thickness varies sufficiently, relative vorticity could be generated from 1  
 2 an adjustment process without any external source. 2

3 The potential vorticity conservation is a key concept for adjustment processes 3  
 4 even in the presence of dissipative forces. Hence, as far as laboratory experiments 4  
 5 on geostrophic adjustment are concerned, it is crucial to perform quantitative 5  
 6 measurements of the potential vorticity field. Such measurements in a rotating 6  
 7 fluid layer are indeed not simple. Both the vorticity field  $\zeta$  and the height field 7  
 8  $\eta$  should be measured simultaneously. If such measurements are now possible, 8  
 9 it is mainly due to recent progress in computers, lasers and cameras technology. 9  
 10 Besides, additional difficulties are encountered on a rotating turntable where 10  
 11 sufficiently compact devices (especially lasers) and remote control of the whole setup 11  
 12 are needed. Therefore, direct measurement of the potential vorticity field is always 12  
 13 challenging for experimentalists. We give below some details on the non-intrusive 13  
 14 methods which can be used to achieve such measurements for specific experimen- 14  
 15 tal configurations. 15  
 16

### 17 2.1. Particle image velocimetry and vorticity field measurements 17

18 The particle image velocimetry (PIV) was developed since 1994 to perform accu- 18  
 19 rate and quantitative measurements of fluid velocity vectors at a very large number 19  
 20 of points simultaneously (Adrian, 2005). Presently, the 2D PIV method consist 20  
 21 to add small neutrally buoyant beads to the working fluid and lightened them with 21  
 22 a laser sheet. The 2D particle motion along this plane are recorded with a digital 22  
 23 video camera. Cross-correlation image processing are then performed to measure 23  
 24 the mean particle displacement in small box region between two successive im- 24  
 25 ages (Fincham and Spedding, 1997). Standard systems are sold by commercial 25  
 26 companies and it is now the most efficient and non-intrusive technique used in 26  
 27 fluid mechanics to obtain a vorticity map in a given region of the flow field. Nev- 27  
 28 ertheless, some technical limitation appears which restrict the spatial resolution 28  
 29 of such measurements in rotating fluid layers. 29  
 30

31 The energy necessary to illuminate fine particles and produce images of suf- 31  
 32 ficient exposure and clarity is the first limitation of PIV. The maximum size of 32  
 33 the measurement window is then fixed by the laser intensity and the camera expo- 33  
 34 sure time. Hopefully, vertical motion are strongly damped in a rotating fluid layer, 34  
 35 therefore neutrally buoyant particles could stay for a relatively long time in a fixed 35  
 36 horizontal plane lightened by the laser sheet. Besides, the horizontal velocities of 36  
 37 geostrophic motions are usually not too large ( $V \simeq 1\text{--}10 \text{ cm s}^{-1}$ ) and the camera 37  
 38 exposure time could be optimized to 10–20 ms. But nevertheless, if the intensity 38  
 39 per unit area is too small the clarity of recorded images may not be sufficient 39  
 40 enough with classical digital camera. On a medium size turntable ( $D \simeq 1 \text{ m}$ ), 40  
 41 high power lasers which require cooling systems are generally excluded. How- 41  
 42 42

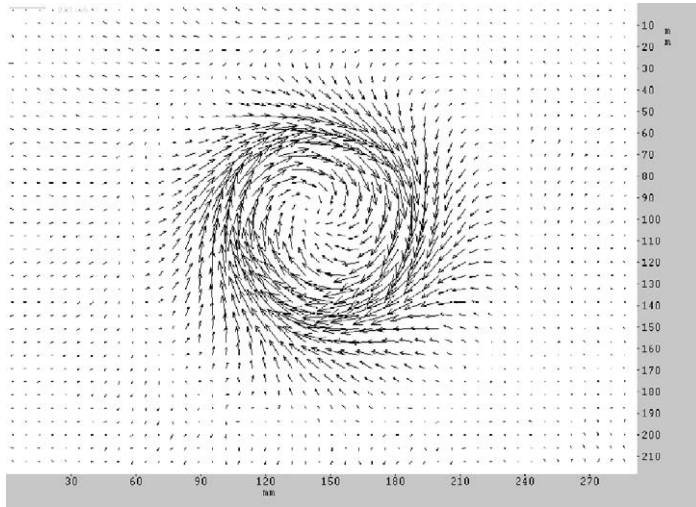


Figure 7. Horizontal velocity field of a cyclone obtained from particle image velocimetry. For clarity, only half of the vectors ( $47 \times 35$ ) are displayed instead of the full ( $94 \times 70$ ) field. The measurement was made in the thin upper layer of a two-layer stratified fluid corresponding to:  $Bu \simeq 0.4$ ,  $\lambda \simeq 0.5$ ,  $\alpha \simeq 0.75$ ,  $\delta \simeq 0.1$ .

ever, the last generation of compact high power laser diodes<sup>2</sup> can generate an uniform intensity line (non-Gaussian) with an output power up to 1 W. With such system we could easily detect the horizontal particle motion ( $V < 10 \text{ cm s}^{-1}$ ) from small ( $10 \text{ cm} \times 10 \text{ cm}$ ) to large ( $1 \text{ m} \times 1 \text{ m}$ ) areas of investigation.

The second limitation is induced by the pixel resolution of the camera. Indeed, to obtain a precise cross-correlation between two interrogation windows, a minimum number of particles ( $\sim 3-5$ ) should be present in the interrogation box. This constraint induces generally a minimum size of a  $8 \times 8$  pixel box. Hence, with a standard  $750 \times 550$  pixels camera we usually get a velocity field of  $95 \times 70$  vectors as it is shown in Figure 8. Using digital cameras with higher resolution ( $3000 \times 2000$  pixels) we could, for instance, reach a  $370 \times 250$  vector grid field. However, even with very high resolution camera and optimized software, PIV measurements will always give a coarse grid resolution in comparison to direct dye tracer visualizations ( $3000 \times 2000$  pixels) or high-resolution numerical simulations ( $4096 \times 4096$  for two-dimensional flows (Bracco, McWilliams, Murante, Provenzale and Weiss, 2000)).

The third limitation comes from the limited precision of the velocity field. Even with hierarchical correlation methods, where correlations deduced from a large interrogation box are used to guide correlation analysis at smaller boxes (Hart,

<sup>2</sup> Lasiris Magnum Laser ([www.laser2000.fr](http://www.laser2000.fr)).

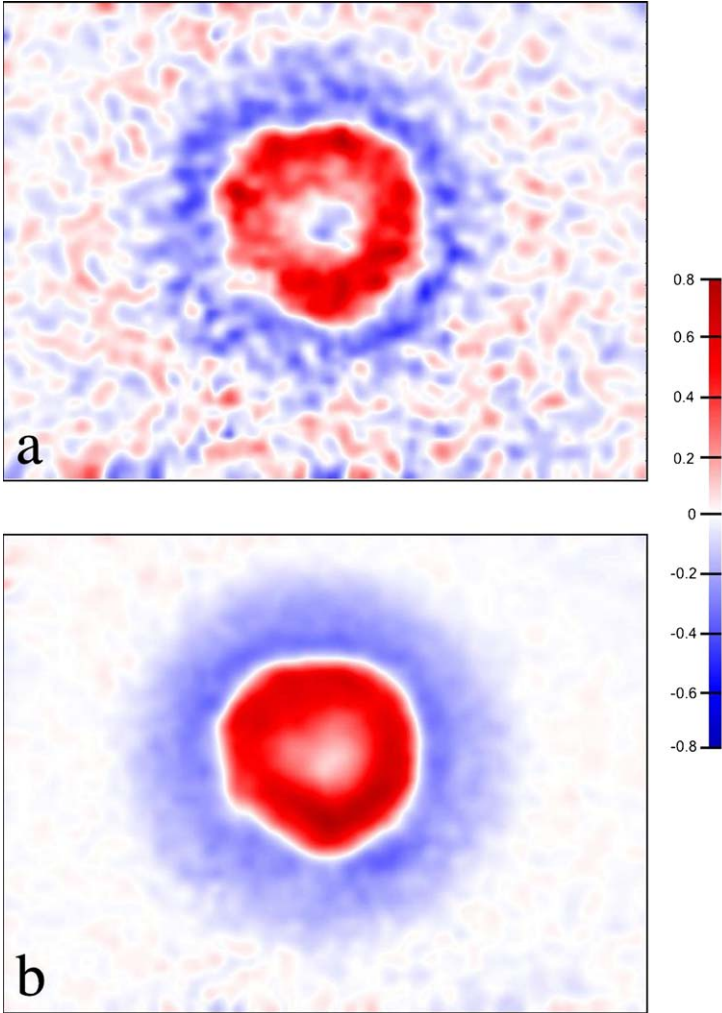


Figure 8. Cyclonic (red) and anticyclonic (blue) dimensionless vorticity  $\zeta/f$  calculated from an instantaneous velocity field (a) or calculated from the time averaged velocity field (b) shown in Figure 8. The Rossby number deduced from the maximum vorticity is about  $Ro = \zeta_{max}/f \simeq 0.6$ . The measurement area is a rectangular window of 280 mm  $\times$  220 mm.

2000), the available dynamical velocity range is about 100:1. In other words, the method cannot detect fluctuations in the velocity field below 1%. Besides, experimental noise on recorded images could easily produces 5% error in the velocity field. This can be a serious problem, because a weak noise in the velocity field

1 induces a stronger noise in the derivatives and therefore strongly influences the  
2 vorticity measurement. Typical errors of order of 10% (or higher) in the vorticity  
3 field could be frequent and strong efforts on the improvement of the image qual-  
4 ity and the software used in the PIV process are needed to reach such precision  
5 on the vorticity field measurements. However, if the flow evolve slowly in compar-  
6 ison with the frequency of the PIV acquisition system, time averaging of the  
7 velocity field is a simple and efficient way to reduce the experimental noise. For  
8 the case of geostrophic adjustment, when a quasi-steady motion is reached, time  
9 averaging will lead to sufficiently precise vorticity measurements. For instance,  
10 the velocity field shown in Figure 8 is an average of ten velocity fields separated  
11 by a time interval of 120 ms. Hence, this corresponds to a time averaged velocity  
12 measurements over 1.2 s which is smaller than the inertial period  $T_f = 12$  s or the  
13 characteristic decay time  $T_E = H_2/\sqrt{v\bar{f}} \simeq 200$  s. Such time averaging reduces  
14 the noise on the vorticity field (Figure 8(b)) by a factor 10 in comparison with the  
15 instantaneous vorticity measurements (Figure 8(a)).

16 According to the above comments, we should emphasize that even if we can  
17 easily obtain a vorticity map from the standard PIV system the accuracy of such  
18 measurements should be checked carefully. Let us recall, that if PIV measure-  
19 ments have a coarse grid resolution corresponding to  $8 \times 8$  or  $12 \times 12$  pixels on the  
20 digitized image, this will be even more pronounced for the vorticity field. Indeed,  
21 to resolve accurately a gradient, at least 3–5 grid points are needed. Therefore,  
22 quantitative vorticity measurements will not be possible if the dynamical struc-  
23 ture under consideration is too small. We can roughly estimate a limiting value as  
24  $25 \times 25$  pixels on the digitized image. Thus, thin vorticity filaments are generally  
25 smoothed by the PIV process. In such case it could be useful to use two cameras  
26 with a wide and a zoom angle in order to quantify accurately the large scale flow  
27 and smaller vortical structures (Perret, Stegner, Farge and Pichon, 2006). Hence,  
28 the standard PIV method is well suited to quantify slow and large-scale struc-  
29 tures in rotating fluid layers. However, for fast and small-scale structures such as  
30 high-frequency waves, this velocimetry method can hardly provide quantitative  
31 measurements, unless an expensive high-speed PIV technology is used.

## 32 2.2. Height field measurements

33 Laboratory techniques for measuring the velocity field, such as the PIV method  
34 described above, are quite advanced. However, methods for making accurate mea-  
35 surements of the height field of a fluid layer have remained relatively elusive. As  
36 far as we know, four non-invasive techniques were used to detect or to measure  
37 the height field fluctuations in rotating fluid layers: light absorption, optical  
38 altimetry from the parabolic free-surface, optical rotation of the working fluid and  
39 laser induced visualization (LIV).  
40  
41  
42

2.2.1. Light absorption

The light absorption technique is based on the optical density of a dyed layer. It consists in measuring the light intensity after absorption through a uniformly dyed fluid layer (Holford and Dalziel, 1996). The fluid layer is usually lightened from below through a transparent vessel while a video camera records the intensity fluctuations from the top (Figure 9(a)). A specific pass-band-filter, which is centered at the maximum absorption of the dye, is put on the video camera to

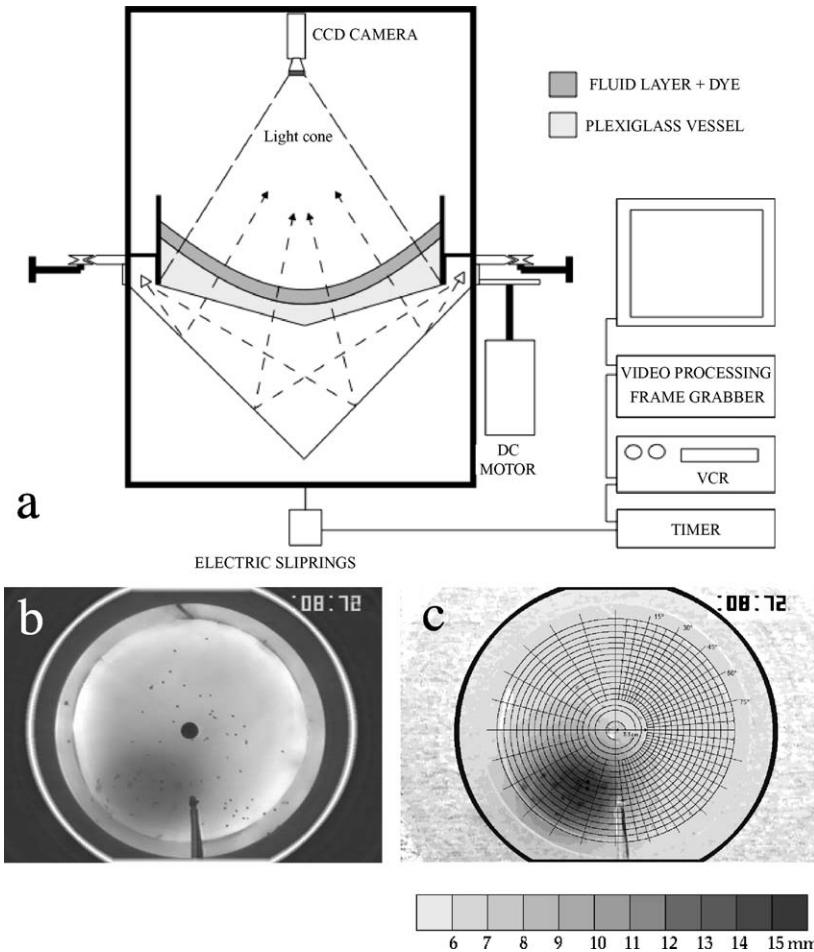
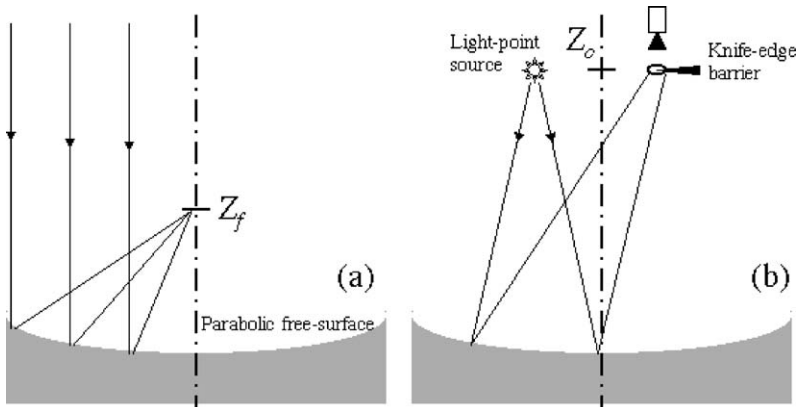


Figure 9. Light absorption technique for a parabolic vessel experiment (a) (Stegner and Zeitlin, 1998). Intensity fluctuations view from the top of the experiment (b) post-processed calibrated image corresponding to a relative elevation  $\lambda \approx 1$  of the layer depth (c).

1 increase the sensitivity. With this method a local increase of the layer thickness  
 2 induces a higher absorption and this region will appear darker on the video image  
 3 (Figure 9(b)). This altimetric measurements was used successfully on small-scale  
 4 parabolic vessel where small (10%) and large (60–100%) relative free-surface devi-  
 5 ation were detected with an accuracy of less than one mm (Stegner and Zeitlin,  
 6 1998). Nevertheless, caustic effects induce systematic errors of order 5–10% of  
 7 the layer thickness which limits the precision on the height measurements.

### 9 2.2.2. Optical altimetry of the parabolic free-surface

10 The free-surface fluctuations of a rotating fluid layer can be imaged and analysed  
 11 using its parabolic free-surface as a Newtonian telescope mirror. Parallel light  
 12 rays from a source high above the rotating table reflects from the water surface  
 13 and converges on the parabolic focus  $Z_f = \frac{1}{2}Z_c$  (Figure 10(a)). However,  
 14 parallel light rays can hardly be obtained on a rotating table. The image of a  
 15 point-light source located at  $Z_c$  (the radius of curvature at the center)  
 16 have sharp focus but converge through a small disk located at the same height  
 17  $Z_c$  (Figure 10(b)). For practical purpose the light source and the camera are sym-  
 18 metrically displayed off the axis. Then, putting a knife-edge barrier in the middle  
 19 of this singular disk, where all the rays converge, can partially obscure the image  
 20 giving great sensitivity to slight imperfections of the reflecting surface. This  
 21 optical altimetry technique is one of the most sensitive method used so far in  
 22 geophysical fluid dynamics experiments. Indeed it is potentially able to detect  
 23 free-surface fluctuations with a one micron precision, independently of the mean  
 24



39 Figure 10. Focusing of parallel light-rays reflected by the parabolic free-surface (a). Sharp conver-  
 40 gence of a point light-source located close to  $Z_c$  the center of curvature of the apex (b). A knife-edge  
 41 barrier induces a contrasted black and white image of the free-surface. It increases the sensitivity to  
 42 deviations from a perfect paraboloid.

1  
2  
3  
4  
5  
6  
7  
8  
9  
10  
11  
12  
13  
14  
15  
16  
17  
18  
19



1  
2  
3  
4  
5  
6  
7  
8  
9  
10  
11  
12  
13  
14  
15  
16  
17  
18  
19

20  
21  
22

Figure 11. Optical altimetry visualisation of inertia-gravity waves (50 μm in amplitude) interacting with a localized vortices. The wave maker is on the bottom left, while the vortices appears in the center. Courtesy Y. Afanasiev.

20  
21  
22

23  
24  
25  
26  
27  
28  
29  
30  
31

thickness of the parabolic layer. Therefore, this method is particularly suited for the investigations of small amplitude waves (less than 0.1% fluctuation) which are often difficult to detect by other methods. For instance, an inertia-gravity wave having an amplitude of 50 μm (0.04% of the mean layer thickness) could be visualized in Figure 11. Qualitative observations of a large variety of dynamical features such as gravity waves, inertial waves, Rossby waves and small-scale convection could then be performed (Rhines, Lindahl and Mendez, 2006; Rhines, 2006).

23  
24  
25  
26  
27  
28  
29  
30  
31

32  
33  
34  
35  
36  
37  
38  
39  
40

Nevertheless, a quantitative method of determination of the slope variation using speckle patterns is possible. A reference image of the fluid layer in solid-body rotation is first made. The slope is measured by comparing the original pattern and a reflected image of this pattern distorted by the surface perturbation induced by the relative flow motion. The procedure is analogous to PIV process where correlations are computed between the small areas of the image and the reference. Nevertheless, the speckle method is limited by large amplitude deformation and have a limited spatial resolution due to the minimum size of the correlation boxes (Rhines, Lindahl and Mendez, 2006; Afanasyev, Rhines and Lindahl, 2006).

32  
33  
34  
35  
36  
37  
38  
39  
40

41  
42

A different quantitative method based on optical color coding was also developed using every pixels of the image. A color slide is fixed just below the

41  
42

1 light source. For a given rotation rate (the null point) the entire surface of water 1  
2 is illuminated by only one color. Any perturbation of the free surface results in 2  
3 the appearance of color different from the null point. It is then possible to mea- 3  
4 sure from each pixel of the image the  $x$  and the  $y$  component of the slope with 4  
5 a 0.1% sensitivity (more details are given in (Afanasyev, Rhines and Lindahl, 5  
6 2006). Hence, by integrating the slope field quantitative height measurements of 6  
7 the parabolic fluid layer could be achieved. 7  
8

### 9 2.2.3. Optical rotation 9

10 An over sophisticated remote sensing method for measuring the thickness of 10  
11 a fluid layer relies upon the optical rotation properties of the working fluid. 11  
12 The liquid is chosen to be optically active (limonene and CFC-113 for instan- 12  
13 ce), so that plane-polarized white light propagating vertically through the 13  
14 fluid layer has its plane of polarization rotated by an angle which depends upon 14  
15 both the wavelength and the layer depth. After leaving the fluid, the angular- 15  
16 dispersed white light passes through a sheet of polaroid. For a given layer 16  
17 depth, only light of a certain wavelength has its polarization axis rotated into 17  
18 exact alignment with the polaroid. Light of other wavelengths is either partially 18  
19 or fully extinguished by the polaroid, giving a correlation between the inter- 19  
20 face height and colour registered by the camera (Hart and Kittelman, 1986; 20  
21 Williams, Read and Haine, 2004). A high-sensitivity up to 1–2% of the layer 21  
22 height could be reached with this technique. Both the large-scale geostrophic 22  
23 flow and small-scale waves could be accurately measured with the technique. 23  
24 According to Figure 12 small-scale fluctuations in the two-layer interface hav- 24  
25 ing 1 to 5 mm amplitude are quantitatively detected. However, the sensitivity 25  
26 will be optimal when the mean rotation angle is about  $90^\circ$  and this implies 26  
27 for the limonene/CFC mixture that the fluid layer should be relatively thick 27  
28  $H = 10\text{--}15$  cm. Besides, specific precautions should be taken to prevent harmful 28  
29 limonene vapours from evaporating into the laboratory. 29  
30

### 31 2.2.4. Laser induced visualization 31

32 Laser induced visualization (LIV) technique could also be used in rotating exper- 32  
33 iments to measure with precision the fluid layer thickness along a line. Initially, 33  
34 the working fluid is uniformly mixed with a fluorescent dye. A vertical laser sheet 34  
35 crosses the horizontal fluid layer and induces the fluorescence of the dye within 35  
36 this plane (Figures 13(a) and 14). In order to optimize the fluorescence, the max- 36  
37 imum of dye absorption  $\lambda_{\text{abs}}$  should be close to the laser wavelength. Hence, 37  
38 we chose the fluoresceine ( $\lambda_{\text{abs}} = 490$  nm) or the Rodhamine 6G ( $\lambda_{\text{abs}} = 530$  nm) 38  
39 if we use, respectively, an argon laser (488 nm) or Nd:Yag laser (532 nm). 39  
40 A video camera, fixed on the side of the tank and perpendicular to the laser 40  
41 sheet could then record the fluorescence of the fluid layer. Using an adequate 41  
42

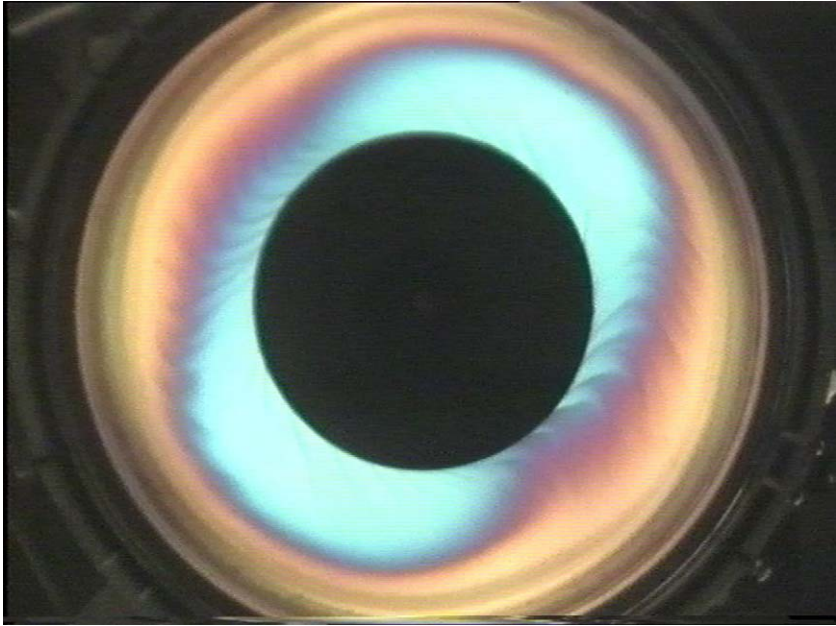


Figure 12. Color calibrated visualisation of the internal interface of a two-layer fluid using optically active CFC-13/limonene for the lower layer. Small-scale waves (5 mm amplitude and 2 cm wave-length) are visible during one cycle of a large-scale and unstable baroclinic mode 2. Courtesy P.D. Williams.

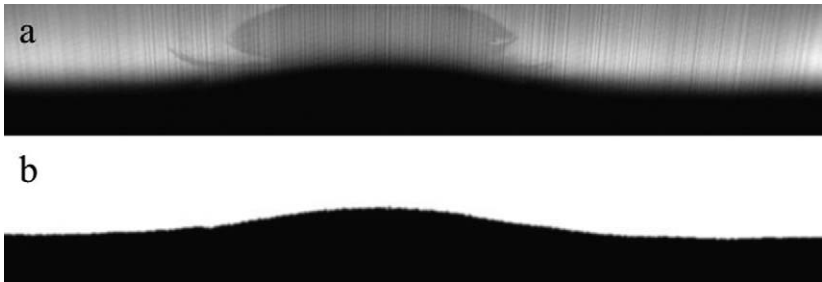


Figure 13. Side view visualization (a) of the fluorescent upper layer. The lower layer appears dark because it does not contain any fluorescent dye and remains therefore transparent to the laser sheet. Edge detection processing (b) allows for a precise measurement of the layer thickness corresponding here to a cyclonic depression:  $Bu \simeq 0.4$ ,  $\lambda \simeq 0.5$ ,  $\alpha \simeq 0.75$ ,  $\delta \simeq 0.1$ .

image processing we then detect the position of the interface between the light fluorescent and the dark transparent fluid (Figure 13(b)). With this non-intrusive technique we were able, for the two-layer configuration, to measure the displace-

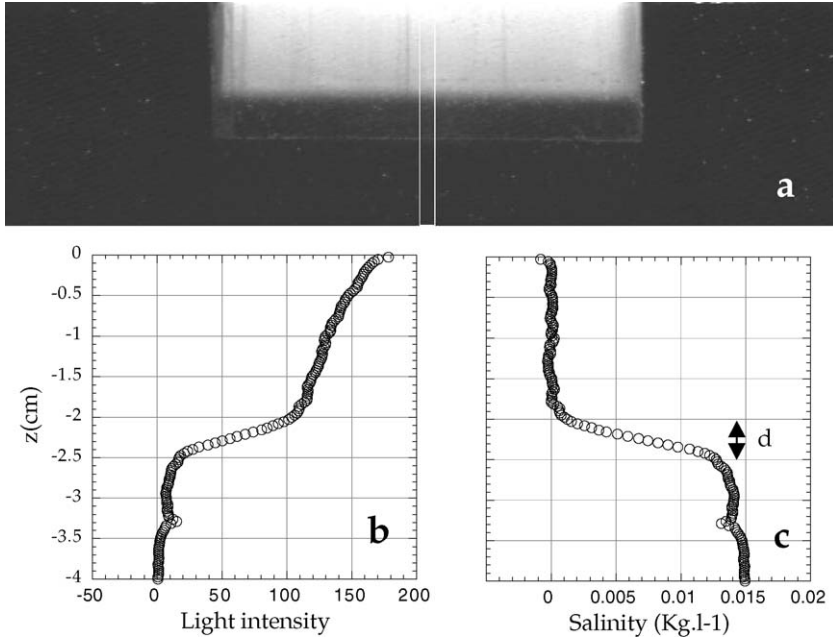


Figure 14. Measurement of the vertical salinity profile from the fluorescent light emission (Stegner, Bouruet-Aubertot and Pichon, 2004). Initially, the upper fluid is uniformly mixed with a fluorescent dye. (a) The upper water initially confined in a transparent bottomless cylinder appears white owing to the fluorescent light emission while the dense water is black. (b) Vertical distribution of the light intensity in the central rectangle shown in (a). (c) The salinity profile can be deduced from (b) if we perform a careful calibration of the laser sheet intensity along the vertical plane. The disturbance at  $z = -3.3$  cm is due to light reflection at the bottom of the cylinder.

ment of the fluid interface between the fresh and the dense water with an accuracy of 2% at fast acquisition rates (Stegner, Bouruet-Aubertot and Pichon, 2004; Perret, Stegner, Farge and Pichon, 2006). The acquisition frequency is limited by the acquisition rate of the camera and the transfer capacity of the video card. A frequency of 100 Hz could be easily reached nowadays with standard firewire cameras. Note in Figure 15 that the LIV camera is not exactly perpendicular to the fluid layers, in order to reduce the image distortion due to the ray diffraction through the stratified interface between the two layers.

Unlike the previous techniques which estimate the height field or its fluctuations in the whole layer, the LIV method gives a measurement of the height field only along a line. Hence, the position of the vertical laser sheet should be carefully chosen. However, this limitation is compensated by the possibility to detect small-scale and three-dimensional structures along the vertical. Indeed, this method measure precisely the dye distribution at each point  $(x, z)$  of a vertical

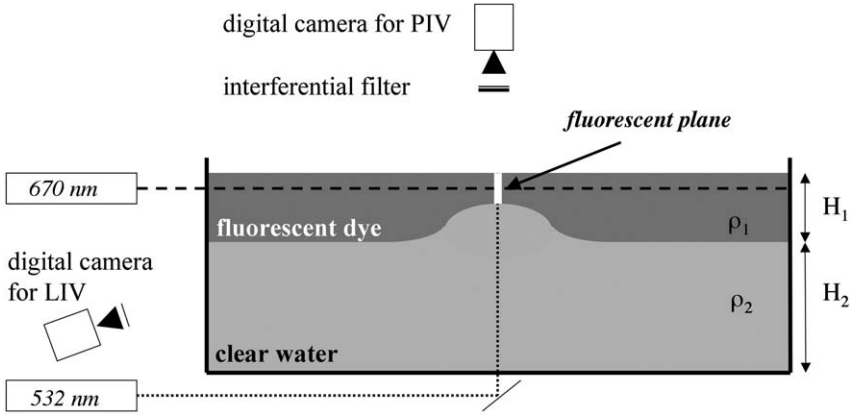


Figure 15. A horizontal red (670 nm) laser sheet with a vertical green (532 nm) laser sheet are used simultaneously in order to couple PIV and LIV measurements in the upper layer.

plane and does not integrate the information along a vertical ray path. Besides, we could also measure the density field from the fluorescent dye emission (Figure 14(a)). Indeed, on short time scale (i.e. few minutes) the mixing of the initial uniform concentration of both dye and salt is expected to be driven mainly by convection (i.e. turbulent mixing). Hence, dye and salt gradient are not affected by relative diffusion and they are therefore proportional. In a first step, we measured the relative fluorescent light emission (Figure 14(b)) which depends mainly on the dye concentration and the laser sheet intensity. Then, taking into account the vertical distribution of the laser sheet intensity, we correlate the light intensity with the local salinity (i.e. density) as shown in Figure 14(c). This could be, in the next future, an efficient non-invasive technique to measure the density field in a continuously stratified fluid.

### 2.3. Potential vorticity measurements

In order to measure the potential vorticity field according to (39) we chose to use both PIV and LIV measurements simultaneously. However, due to the restrictions of the LIV technique, which gives the height field only along a line, the coupling of these non-invasive methods is best suited for unidirectional flows. It is then possible from a line measurement to estimate a global potential vorticity field for either circular (Stegner, Bouruet-Aubertot and Pichon, 2004) or parallel flows (Perret, Stegner, Farge and Pichon, 2006). A typical experimental setup for a circular cyclonic PV anomaly is shown Figure 15. Two lasers having different wavelengths are used in addition with specific optical filters, fixed on each cam-

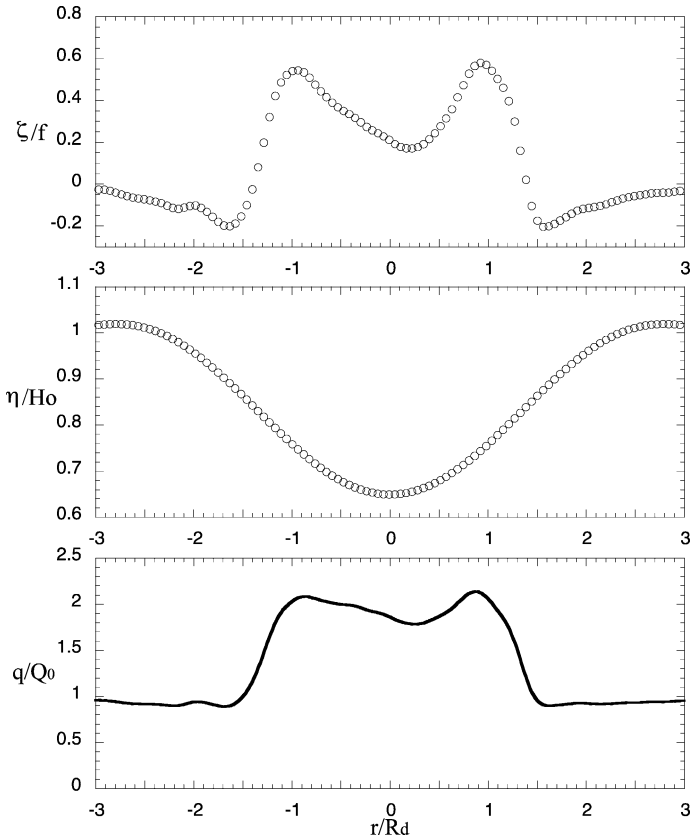


Figure 16. Plots of the averaged vorticity profile measured by PIV (a) and the averaged height profile (b) measured by LIV corresponding to the mean steady state at  $t = 2T_f$ . The potential vorticity (c) is deduced from these two profiles. These measurements correspond to the same cyclonic PV anomaly shown in Figures 8(b) and 13.

era, in order to detect the dye emission only in the vertical plane and the buoyant particles only in the horizontal plane.

Time averaged vorticity and height profiles along a diameter are displayed in Figure 18. These profiles corresponds to the PIV and LIV measurements shown in Figures 8(b) and 13. The temporal averaging (over one inertial period  $T_f = 2\pi/f$ ) filters out the fast wave motion from both the density interface and the azimuthal horizontal velocity. Hence, these profiles correspond to the mean adjusted state of the system which evolves slowly in comparison with the wave motion. From these data we can then easily quantify the potential vorticity (Figure 16(c)) of the cyclonic PV anomaly. The PV profile is rescaled here

1 by  $Q_0 = f/H_1$ , the intrinsic PV of the unperturbed upper fluid layer (solid line 1  
 2 in Figure 16(c)). For this case, the initial circular PV anomaly was a constant  $Q$  2  
 3 patch with  $Q/Q_0 = 2$ . 3

4 As far as we know, this technique is the first attempt for direct and quantitative 4  
 5 measurements of the potential vorticity field in a rotating shallow-water layer ex- 5  
 6 periment. In other laboratory studies, either the height field or the velocity field 6  
 7 were measured but not both of them simultaneously. In such case, the “missing” 7  
 8 field could be estimated according to the geostrophic or cyclo-geostrophic bal- 8  
 9 ance and the potential vorticity field reconstructed. Nevertheless, these indirect 9  
 10 methods could induce significant errors especially when ageostrophic or non- 10  
 11 hydrostatic motions become non negligible. A more refined method based on data 11  
 12 assimilation was used recently (Thivolle-Cazat, Sommeria and Galmiche, 2005). 12  
 13 The experimental results were compared with a two-layer isopycnal model and 13  
 14 data assimilation was used to extrapolate from PIV measurements both the in- 14  
 15 terface position and the potential vorticity field. However, such PV extrapolation 15  
 16 depends strongly on the underlying assumptions of the numerical model used and 16  
 17 on the assimilation scheme. Therefore, we do believe that coupled measurements 17  
 18 is the best way to quantify the PV. Nevertheless, data assimilation will fully ben- 18  
 19 efit from these coupled measurements and it could become an optimal method to 19  
 20 test the limits of validity of the shallow-water modelisation for real flows. 20  
 21

### 22 **3. Simple case studies of geostrophic adjustment** 22

23 We describe in what follows few cases of geostrophic adjustment based on lock 23  
 24 released experiments performed in rotating fluids. In a two-layer configuration, 24  
 25 vertical boundaries (i.e. locks) are used to fix initial height (or density) steps, 25  
 26 in the upper layer. For such cases when there is no relative motion in the layers 26  
 27 the initial PV field is precisely controlled by the layer thickness. If the release of 27  
 28 the vertical walls is rapid enough, we could then follow the geostrophic adjustment 28  
 29 of a well defined initial condition corresponding to discontinuous profiles of con- 29  
 30 stant PV. The simplicity of the initial condition makes these experiments easily 30  
 31 reproducible. 31  
 32

#### 33 *3.1. “Warm-core” lens* 33

##### 34 *3.1.1. Initial state and experimental configuration* 34

35 The term warm-core lens is generally used for mesoscale vortices which contain a 35  
 36 finite volume of warm and light water at the ocean surface. A simple experimental 36  
 37 configuration leads to similar dynamical structure (Griffiths and Linden, 1981; 37  
 38 Rubino and Brandt, 2003). A fixed volume of buoyant water is initially confined 38  
 39 within a bottomless cylinder of radius  $R_c$  on the top of a dense rotating fluid 39  
 40 41  
 42

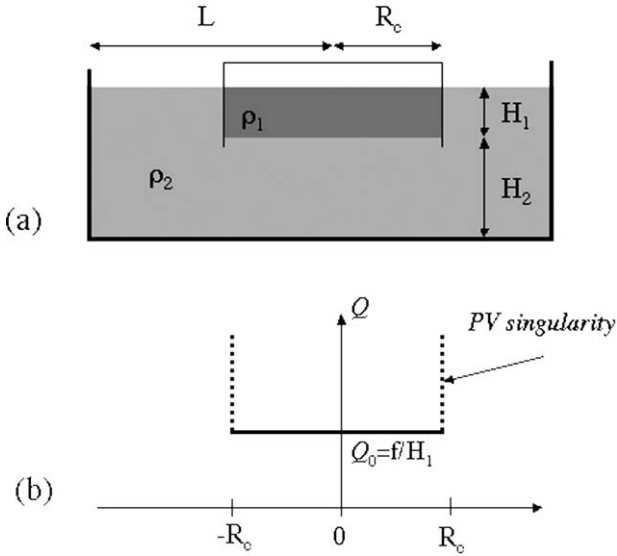


Figure 17. Initial configuration of the “warm-core” lens: the setup (a), and the initial profile of the corresponding potential vorticity (b).

(Figure 17(a)). Assuming that the thin upper layer follows the reduced-gravity RSW equations (cf. Chapter 1), the initial PV distribution is constant for  $r < R_c$  and exhibit a singularity at  $r = R_c$  (Figure 17(b)) due to the vanishing layer thickness. Similar experiments were performed to study the baroclinic instability of a density front leading to meanders and eddies (Griffiths and Linden, 1981; Bouruet-Aubertot and Linden, 2002). The present experiment was made with a smaller thickness ratio parameter  $\delta \simeq 0.1$  to reduce the growth rate of baroclinic disturbances and focus the study on the adjustment process (Stegner, Bouruet-Aubertot and Pichon, 2004).

### 3.1.2. Dynamical stages

Three stages were observed during the adjustment process. Just after the rapid withdrawal of the transparent cylinder, the fresh water spreads radially as a gravity current. During this initial stage, the flow is fully three-dimensional (Figure 18(a)) and the effects of rotation are expected to be weak. After approximately half of the inertial period, the radial extension of the lens is stopped (Ungarish and Huppert, 1998). The second stage corresponds to a radial contraction of the lens where steep jumps at the interface may appear (Figure 18(b)). Then, after about two inertial periods, the density front reaches an equilibrium characterized by a standing wave mode superimposed on the mean state (Figures 18(c), (d)). In all our exper-

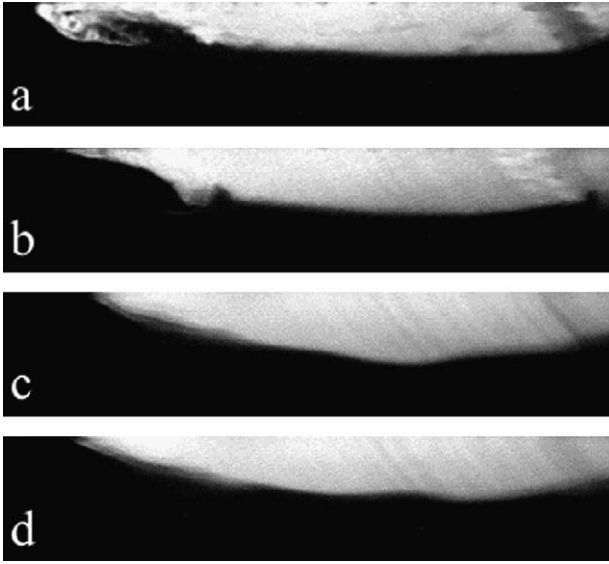


Figure 18. Dynamical evolution of the interface for the initial configuration corresponding to  $Bu = (R_d/R_c)^2 \simeq 0.4$ ;  $\alpha \simeq 0.76$ ;  $\delta \simeq 0.08$  (Stegner, Bouruet-Aubertot and Pichon, 2004). The snapshots are taken at  $t = 0.5T_f$  (a),  $t = 0.8T_f$  (b),  $t = 3T_f$  (c) and  $t = 0.5T_f$  (d). The dark rays on the right hand side of the image are experimental shadows produced by the upper fixations of the cylinder.

iments, this third stage is rapidly reached after approximately one or two inertial periods. These results agree with previous studies (Mahalov, Pacheco, Voropayev, et al., 2000) who also found that the inertial period is the characteristic time of the transition from a density current to a geostrophic front.

### 3.1.3. Rotating shallow-water predictions

We present here the approximations and the calculation of classical Rossby adjustment theory for the axisymmetric warm-core lens configuration (Figure 17). According to the small thickness ratio parameter  $\delta \simeq 0.1$  and the weak motion observed in the lower layer  $Ro^{(2)} \simeq \delta Ro^{(1)}$  (Stegner, Bouruet-Aubertot and Pichon, 2004) the reduced gravity RSW equations are expected to provide, in first order of approximation, an accurate description of the upper layer dynamics. Besides, we assume that viscosity and dissipative effects are negligible and that the system reaches a final steady state. Using the deformation radius as the characteristic horizontal scale (i.e.  $Ro = 1$  and  $\lambda = 1$ ) we get the following dimensionless cyclo-geostrophic balance for an axisymmetric steady state:

$$\frac{v^2}{r} + v = \partial_r \eta. \quad (41)$$

The Lagrangian conservation of PV implies a constant value for all fluid parcel within the upper lens:

$$Q(r \geq r_f) = 1 = \frac{1 + \partial_r v + v/r}{1 + \eta} \quad (42)$$

where  $r_f$  is the final radius of the density lens. According to (41) and (42) we get:

$$\frac{1}{r} \partial_r (r \partial_r v) - \frac{v}{r^2} - \left( v + \frac{v^2}{r} \right) = 0 \quad (43)$$

with the boundary conditions

$$v(0) = 0, \quad (44)$$

$$h(r_f) = 1 + \eta(r_f) = 0 \quad \Rightarrow \quad \left( \partial_r v + \frac{v}{r} + 1 \right) (r_f) = 0. \quad (45)$$

For a given radius  $r_f$ , we can solve (43), (44) and (45) numerically with standard shooting methods. Then, the angular momentum conservation or mass conservation or mass conservation both give the same implicit relation between  $r_f$  and the initial radius of the cylinder  $r_c$ :

$$r_c^2 = r_f^2 + 2r_f v(r_f) \quad (46)$$

The velocity  $v(r)$  and the height  $h(r)$  profiles of the steady adjusted density lens are fixed by a single parameter  $r_c = R_c/R_d = Bu^{-1/2}$ . Examples of velocities and height profiles are given in Figure 21 for the same initial state and two different deformation radii corresponding to  $Bu = 0.05$  and  $Bu = 5$ . For small Burger number we expect an axisymmetric jet (or large-scale ring) whereas for large Burgers number an eddy (close to solid rotation) is expected.

### 3.1.4. Mean adjusted state

In the warm-core lens configuration, the interface between the two fluids intersects the free surface. Hence, unlike the standard Rossby adjustment problem (Gill, 1982; Vallis, 2006) inertia-gravity waves cannot propagate away from the region of the initial density anomaly. Therefore, the separation between the adjusted state and the wave motion is not direct. Hence, we used time averaging over one or two  $T_f$ , as described in the previous section (Section 2), in order to extract the slow dynamics of the height profile and the velocity field. We first observe that the averaged height profile, displayed in Figure 20(a), remain almost constant between  $t \simeq 1.5T_f$  and  $t \simeq 7T_f$ . During that time, the averaged velocity profile experiences a slow dissipation (Figure 20(b)). Therefore, even if a strong wave activity is present according to Figure 18, the averaged mean state remains quasi-steady after one or two inertial periods. Moreover, in the central region, this

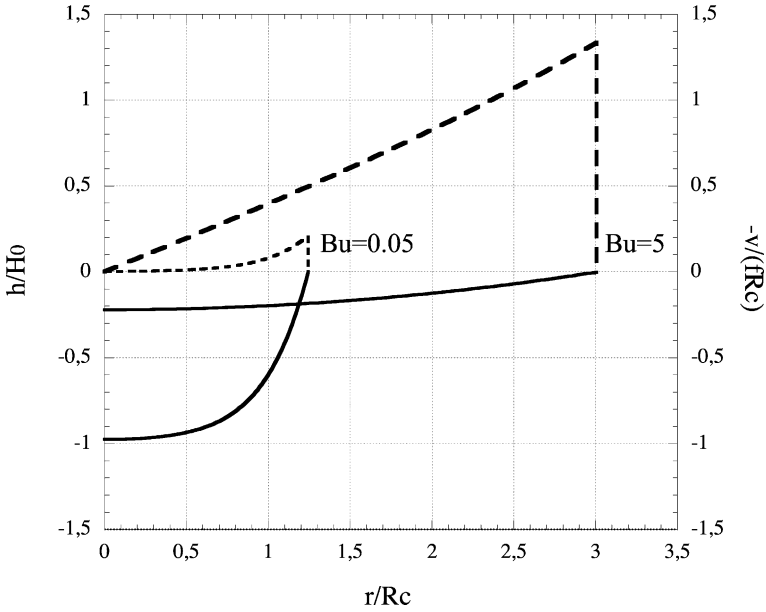


Figure 19. Final steady state according to the standard Rossby adjustment. Two adjusted velocity (dashed line) and height (solid line) profiles resulting from the same initial density anomaly ( $h = H_1$ ,  $r = R_c$ ) are plotted for two different deformation radii  $Bu = 0.05$  and  $Bu = 5$ .

quasi-steady state is relatively close to the cyclo-geostrophic adjusted state predicted by the PV conservation in the RSW framework. According to this inviscid adjustment model the velocity reaches its maximum and is discontinuous at the edge of the lens. This is obviously unrealistic in a physical system where dissipative processes occur. Indeed, according to Figure 20(b) the maximum velocity is almost three times smaller than the predicted one. Hence, both the velocity and the potential vorticity of these anticyclonic lenses are smoothed near the edge front over a characteristic distance equal to the deformation radius (in the present case  $R_d = 3.2$  cm while  $R_c = 5.25$  cm).

### 3.1.5. Small-scale instabilities

Detailed analysis of the velocity field evolution show that strong and localized dissipation occurs in the very initial stage of adjustment ( $t \leq 2T_f$ ) while the flow experiences only a weak dissipation afterwards. This rapid dissipation which occurs at the edge of the anticyclonic lenses induces a significant deficit in the kinetic energy of the adjusted flow up to 50% or 80% (Stegner, Bouruet-Aubertot and Pichon, 2004). Dye visualization reveals that transient and rapid three-dimensional instabilities occur in the very first stage of adjustment (Figure 21).

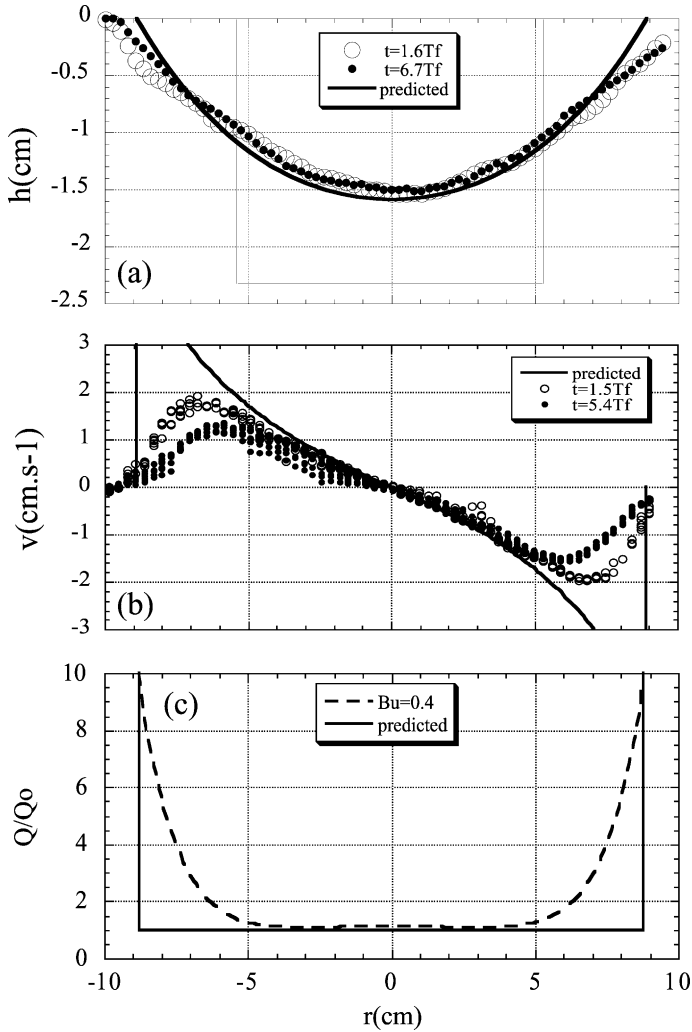


Figure 20. Mean height (a), velocity (b) and PV (c) profiles averaged over one inertial period. The initial density anomaly confined within the bottomless cylinder is plotted with a thin line in (a). The thick solid line corresponds to the cyclo-geostrophic adjusted state predicted by the geostrophic adjustment scenario of the inviscid RSW model.

A first unstable perturbation having a short wavelength grows very quickly, then spiralling arms appear with a larger wavelength. The first instability scales with the viscous diffusion length  $L_v = \sqrt{\nu T_f} \simeq 3-4$  mm and does not depend on the Burger number while the secondary mode corresponding to the spiralling

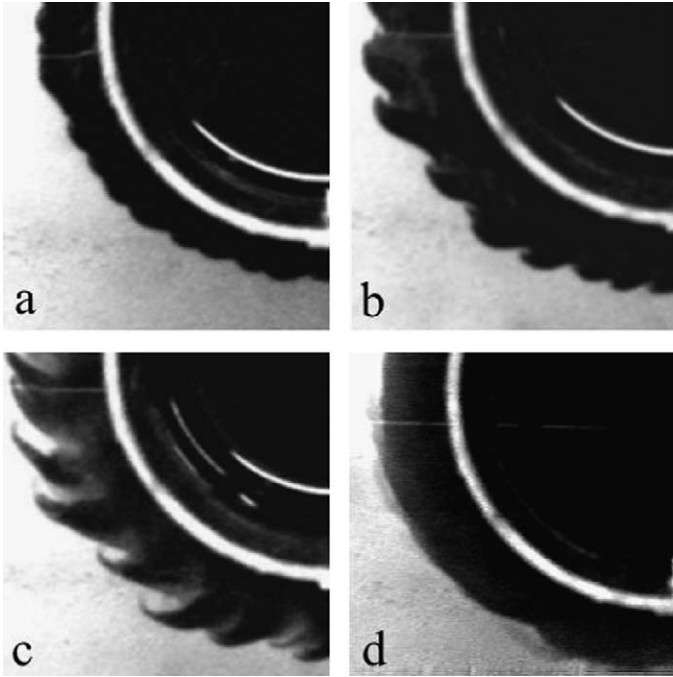


Figure 21. Dye visualization of the three-dimensional perturbations at the edge of the anticyclonic lens (a)  $t = 0.3T_f$ , (b)  $t = 0.5T_f$ , (c)  $t = 0.7T_f$  and (d)  $t = 1.7T_f$  (Stegner, Bouruet-Aubertot and Pichon, 2004).

arms does scale with the deformation radius. These three-dimensional instabilities localized in time (less than one inertial period) and space (the edge of the anticyclonic lens) provide an efficient mechanism of turbulent dissipation which cascades energy toward small scales in the frontal region. However, outside the outcropping region the potential vorticity conservation is well verified.

### 3.2. Cyclonic and anticyclonic PV patches

#### 3.2.1. Initial state and experimental configuration

We used the term “PV patches” for localised positive or negative potential vorticity anomalies of constant values within a uniform PV layer. The “PV patch” model is the generalisation of the Rankine vortex (cylindrical vorticity patch) for a rotating shallow-water layer. It is the simplest description of potential vorticity front with no outcropping. It could be, for instance, a simplified description of the cyclonic polar vortex in the stratosphere. The corresponding experimental configurations for anticyclonic and cyclonic “PV patches” are shown respectively

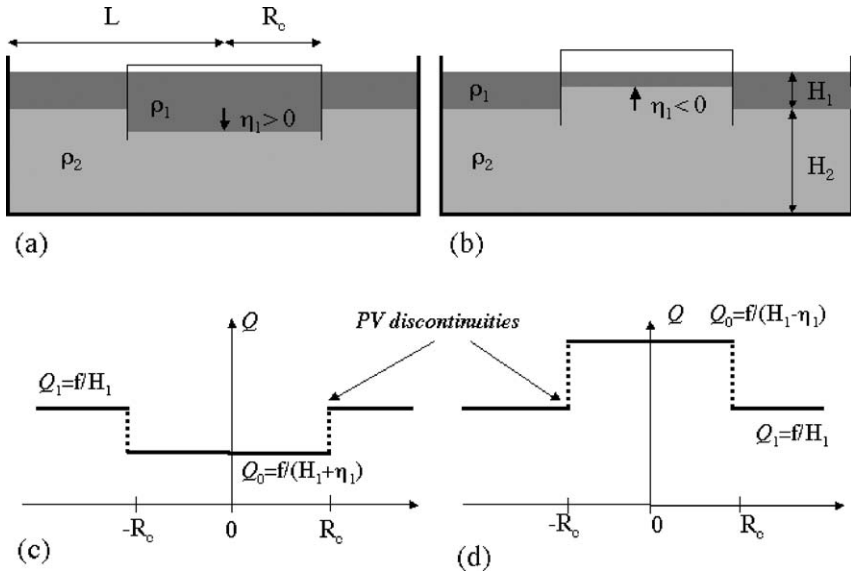


Figure 22. Initial configuration of the experimental setup corresponding to an anticyclonic (a) and a cyclonic (b) PV patch and their respective PV profiles (c) and (d).

in Figures 23(a) and 23(b). A two-layer stratification with a small thickness parameter  $\delta = 0.125$  is first realized. Then, a bottomless cylinder is used to produced an height step in the two-layer interface. Assuming that the thin upper layer follows the reduced-gravity RSW equations, the initial PV distribution is uniform inside ( $r < R_c$ ) and outside ( $r > R_c$ ) the cylinder. Unlike, the “warm core” lens configuration (Figure 17) the potential vorticity exhibit a discontinuity (but not a singularity) at  $r = R_c$  due to the finite jump in the layer thickness. Besides, both positive and negative circular PV jumps could be obtain (Figures 23(b), (c)). A positive (negative) thickness anomaly in the upper layer correspond to a negative (positive) PV jump and will generally lead to a localized anticyclonic (cyclonic) circular ring or vortex.

### 3.2.2. Dynamical stages

The very initial stage of adjustment differs from the warm-core lens configuration. Just after the withdrawal of the transparent cylinder, the vertical density jump get tilted and a local overturning motion is initiated at the initial position of the cylindrical wall. However, due to the rotation, the overturning motion is stopped after one inertial period and a localized shock (steep density front) occurs as shown in Figures 23(b) and 24(b). Due to the absence of outcropping front no gravity current head is visible for the PV-patch configuration. Afterwards, the thickness

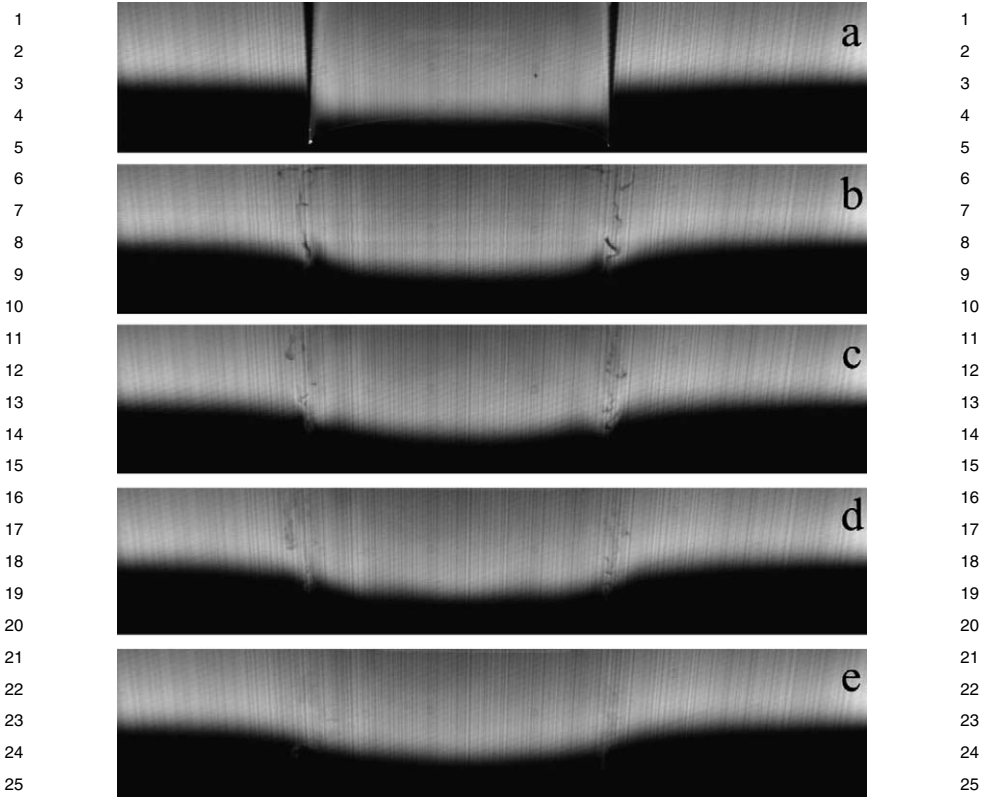


Figure 23. Dynamical evolution of the interface of an anticyclonic PV patch corresponding to  $Bu = (R_d/R_c)^2 \simeq 0.084$ ;  $\lambda = 0.5$ ;  $\alpha^{(1)} \simeq 1.6$ ;  $\delta \simeq 0.125$ . The snapshots are taken at (a)  $t = 0$ , (b)  $t = T_f$ , (c)  $t = 2T_f$ , (d)  $t = 3T_f$  and (e)  $t = 10T_f$ .

anomaly reaches an equilibrium. Even if, small fluctuations could be detected this mean adjusted state holds for a relatively long time. According to Figures 23(c)–(e) and 24(c)–(e), for a small Burger number configuration (here  $Bu = 0.084$ ) the amplitude and size of the mean adjusted state remain close to the initial unbalanced height profile. Besides, the thickness anomaly remain almost unchanged from  $t = 2T_f$  to  $t = 20T_f$ . Hence, the system reaches a quasi-steady state in a very short time, approximately one or two inertial periods. For higher Burger numbers, the amplitude of the fluctuations is larger and the system seems to be far from an equilibrium. However, using an accurate time averaging to filter out the fast wave motion (see below), an averaged mean state is reached with the same rapidity. This characteristic time for adjustment (one or two inertial periods) does not depends on the size or the amplitude of the initial PV-patch.

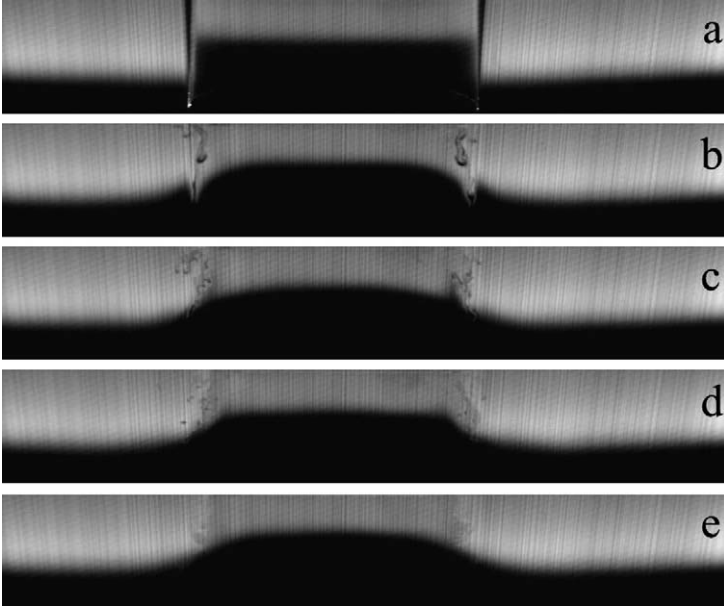


Figure 24. Dynamical evolution of the interface of a cyclonic PV patch corresponding to  $Bu = (R_d/R_c)^2 \simeq 0.084$ ;  $\lambda = -0.5$ ;  $\alpha^{(1)} \simeq 1.6$ ;  $\delta \simeq 0.125$ . The snapshots are taken at (a)  $t = 0$ , (b)  $t = T_f$ , (c)  $t = 2T_f$ , (d)  $t = 3T_f$  and (e)  $t = 10T_f$ .

### 3.2.3. Rotating shallow-water predictions

We present here the calculation of classical Rossby adjustment theory for the cylindrical “PV-patch” configuration (Figure 22). As for the “warm-core” lens case, the small thickness ratio and weak motions in the lower layer justify to use the reduced gravity RSW equations for the upper layer dynamics. Here again we neglect, at the first order of approximation, the dissipation. Therefore, we use the same set of dimensionless equations as the “warm-core” lens configuration, but we need to consider two distinct regions of uniform PV. We will use the index 0 for the inner PV anomaly region ( $r < r_f$ ) and the index 1 for the outer region ( $r > r_f$ ) where  $r_f$  is the radial position of the PV jump in the final adjusted state. For the case of an anticyclonic PV patch (Figure 22(c)) we expect a radial extension of the PV front ( $r_c < r_f$ ) while for the cyclonic PV patch (Figure 22(d)) we expect a radial contraction ( $r_f < r_c$ ). The Lagrangian conservation of potential vorticity implies a constant but distinct value of PV for all fluid parcel within each region of the upper fluid layer. Hence, for the inner PV anomaly region we have:

$$Q_0(r < r_f) = \frac{1}{1 + \lambda} = \frac{1 + \partial_r v_0 + v_0/r}{h_0} \quad (47)$$

1 while for the outer region we have: 1

$$2 \quad Q_1(r > r_f) = 1 = \frac{1 + \partial_r v_1 + v_1/r}{h_1} \quad (48) \quad 2$$

3 where the relative PV anomaly is given initially by  $\lambda = \eta_1/H_1$ . 3

4 Then, looking for a steady adjusted state, implies the cyclo-geostrophic bal- 4  
 5 ance (41) and according to (47)–(48) we get the second order non-linear ordinary 5  
 6 differential equations: 6

$$7 \quad \frac{1}{r} \partial_r (r \partial_r v_i) - \frac{v_i}{r^2} - Q_i \left( v_i + \frac{v_i^2}{r} \right) = 0 \quad (49) \quad 7$$

8 with the boundary conditions: 8

$$9 \quad v_0(0) = 0, \quad (50) \quad 9$$

$$10 \quad v_0(r_f) = v_1(r_f), \quad (51) \quad 10$$

$$11 \quad h_0(r_f) = h_1(r_f) \Rightarrow \quad 11$$

$$12 \quad (1 + \lambda) \left( \partial_r v_0 + \frac{v_0}{r} + 1 \right) (r_f) = \left( \partial_r v_1 + \frac{v_1}{r} + 1 \right) (r_f). \quad (52) \quad 12$$

13 Besides, far away from the potential vorticity front ( $r \gg r_f$ ), a localized solu- 13  
 14 tion satisfy the geostrophic balance which implies to neglect the non-linear term 14  
 15 in (49). In such case, the general solution of the linearized equation (49) is ex- 15  
 16 pressed through Bessel functions. The outer velocity of a localized adjusted state 16  
 17 should then decay at infinity as a modified Bessel function of the second kind 17

$$18 \quad v_1(r \rightarrow +\infty) \propto K_1(r). \quad (53) \quad 18$$

19 For a given radius  $r_f$ , we can solve equations (49)–(53) numerically with ap- 19  
 20 propriate shooting methods. Then, as for the “warm-core” lens configuration, the 20  
 21 angular momentum conservation leads to the same implicit relation (46) between 21  
 22  $r_f$  and the initial position of the front  $r_c$  (i.e. the dimensionless cylinder radius). 22  
 23 The velocity and the height profiles of the steady adjusted PV-patch are then fixed 23  
 24 by two dimensionless parameter:  $r_c = R_c/R_d = Bu^{-1/2}$  and  $\lambda = \eta_1/H_1$ . Exam- 24  
 25 ples of velocities and height profiles for both cyclonic and anticyclonic PV patches 25  
 26 are given in Figure 25. For large Burger number, in other words a small cylinder 26  
 27 radius in comparison with the deformation radius, the adjusted state correspond 27  
 28 to a localized vortex (Figure 25(a)). The velocity profile exhibit a core solid ro- 28  
 29 tation analogous to Rankine vortices. For small Burger number (Figure 25(b)), 29  
 30 the adjusted state correspond to a circular jet (i.e. circular velocity ring). For 30  
 31 all these cases, the maximum velocity radius corresponds to  $r_f$  the final posi- 31  
 32 tion of the PV jump. Unlike, the “warm-core” lens configuration, the velocity 32  
 33 33  
 34  
 35  
 36  
 37  
 38  
 39  
 40  
 41  
 42

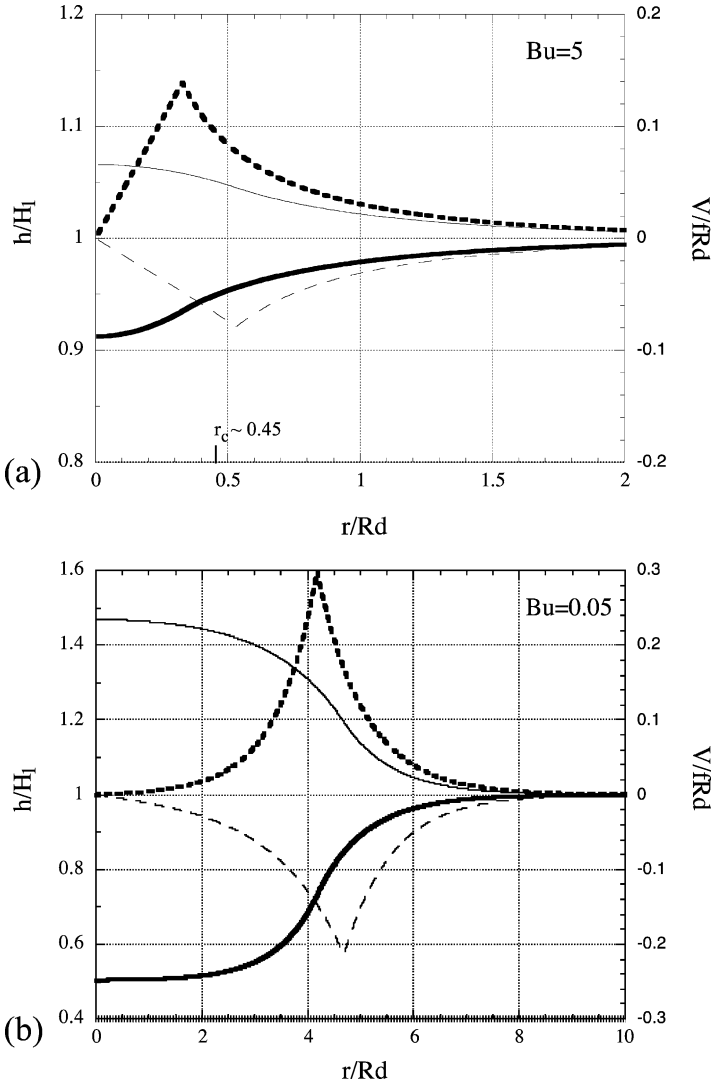


Figure 25. Velocity (dashed lines) and thickness profiles (solid lines) predicted by the standard geostrophic adjustment for two different sizes of the initial PV patch:  $r_c = R_c/R_d \simeq 0.45$  (a) and  $r_c = R_c/R_d \simeq 4.47$  (b). The anticyclonic (thin line) and the cyclonic (thick line) profiles are given respectively for  $\lambda = 0.5$  and  $\lambda = -0.5$ .

profiles for PV-patches are always continuous. Besides, in agreement with previous studies (Kuo and Polvani, 2000), the geostrophic adjustment process induce a cyclone–anticyclone asymmetry. For the same amplitude of the initial poten-

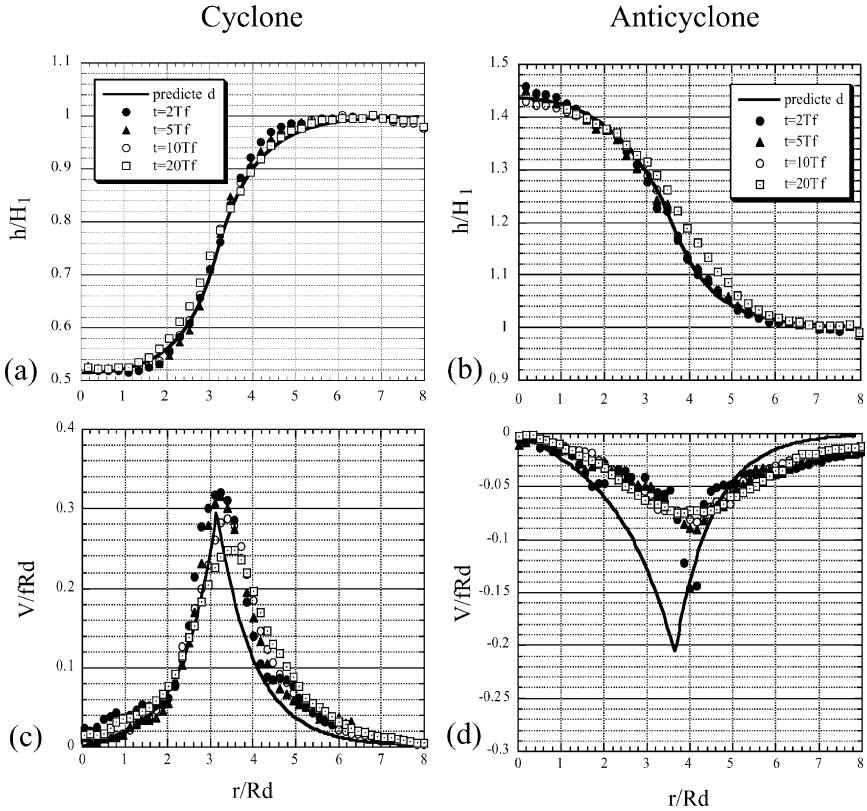


Figure 26. Profiles of the upper layer thickness for a cyclonic (a) and an anticyclonic (b) vortex resulting from the initial PV-patch  $r_c = R_c/R_d \simeq 3.47$  ( $Bu = 0.083$ ) and  $\lambda = 0.5$  or  $\lambda = -0.5$ . The corresponding velocity profiles are displayed in (c) and (d). All the profiles were time-averaged over one inertial period  $T_f$ . These mean profiles are shown at various time:  $t = 2T_f$  (filled circle),  $t = 5T_f$  (filled triangle),  $t = 10T_f$  (open circle) and  $t = 20T_f$  (open square).

tial energy fluctuation, the cyclonic structures will be here more intense than the anticyclonic ones. Indeed, according to Figure 25, for the same relative amplitude of the initial thickness anomaly, the maximum velocity of cyclonic vortices ( $v_{\max}/(fR_d) = 0.3$  for  $\lambda = -0.5$  and  $r_c = 4.47$ ) will always be higher than the anticyclonic ones ( $v_{\max}/(fR_d) = -0.2$  for  $\lambda = 0.5$  and  $r_c = 4.47$ ).

### 3.2.4. Mean adjusted state

As for the warm-core lens configuration, we used time averaging over one or two inertial period  $T_f$  in order to extract the slow dynamics of the height profile and the velocity field. According to Figure 26, we observe that both the mean height

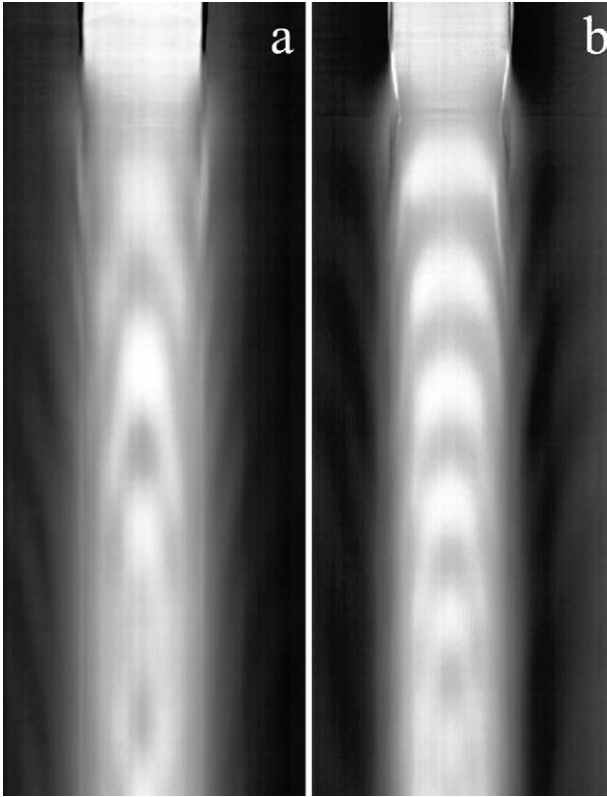


Figure 27. Spatio-temporal diagram of the relative fluctuations of the upper layer thickness for an anticyclonic (a) and a cyclonic (b) PV patch. The time evolve along the  $y$  axis from top ( $t = 0$ ) to bottom ( $t = 7T_f$ ), while the layer thickness is plotted along the  $x$  axis corresponding to a full length of 260 mm. The grayscale levels were decalibrated and intensified in order to enhance the contrast. The white rectangular area on both panels corresponds to the initial positive ( $\lambda = 0.5$ ) or negative ( $\lambda = -0.5$ ) height anomaly.

and the velocity profiles remain almost constant for several inertial periods, at least up to  $20T_f$  for PV-patches having small Burger number values ( $Bu = 0.083$  in Figure 26). Hence, the time-averaged state have reached an equilibrium even if small wave motion could be detected both in the inner region of the PV anomaly (Figure 27) and the outer region. For the cyclonic structure, the mean-adjusted state coincide perfectly with the predictions of standard geostrophic adjustment (Figures 26(a), (c)). However, for the anticyclonic structure a significant discrepancy occurs for the velocity field (Figure 26(d)). The maximum velocity is at least two times smaller than the predicted one. This anticyclonic dissipation, in compar-

ison with the non-dissipative predicted state, was observed in all the experiments from small to large Burger numbers  $Bu = r_c^{-2}$ . Hence, the cyclone-anticyclone asymmetry becomes even more pronounced with this unpredicted dissipation. As for the warm-core lens configuration (which corresponds to the asymptotic limit  $\lambda \rightarrow +\infty$ ), we could suspect that this rapid dissipation of kinetic energy is due to a transient three-dimensional instability which affects only the anticyclonic PV fronts. However, dye visualisations appeared to be less efficient for the PV-patch experiments and we could hardly capture small-scale perturbations. We should note that an outcropping PV front (PV singularity) lead to intense velocities ( $Ro \simeq 1$ ) in comparison with PV-step front (PV discontinuity) which induce continuous velocity field close to the geostrophic balance. Indeed, the Rossby number never exceed  $Ro = 0.3$  in the PV-patch experiment, therefore ageostrophic motions and related instabilities are expected to be weaker than for the outcropping configuration.

### 3.2.5. Inertial and sub-inertial wave activity

The geostrophic adjustment process is expected to transfer a small (large) amount of the initial potential energy to the fast wave motion for PV-patches having small (large) Burger number corresponding to  $r_c = R_c/R_d > 1$  ( $r_c < 1$ ). Hence, for the small Burger number case described above  $Bu = 0.083$ , the amplitude of the wave fluctuations were about few percents of the mean upper layer thickness. The sensitivity of the LIF technique was high enough to quantify this wave activity in the inner region (inside the PV anomaly) and in the outer region. Spatio-temporal diagrams (i.e. Hovmöller plots) of the wave oscillations within the cyclonic and the anticyclonic PV patch are rendered [Figure 27](#). This plot shows qualitatively the temporal variations ( $y$  axis) of the upper layer thickness across a diameter ( $x$  axis). The grayscale levels were decalibrated and intensified in order to enhance the contrast for a better visualisation. Unlike the outcropping configuration, the two-layer interface extend here in the whole experimental domain and the inertia-gravity waves could freely propagate in the outer region outside the PV anomaly. Nevertheless, a significant wave activity remain for a long time (several inertial period) inside the PV anomaly even if the mean steady state is already adjusted ([Figure 26](#)). A similar behavior was found in previous theoretical ([Plougonven and Zeitlin, 2005](#)) and numerical ([Kuo and Polvani, 2000](#)) studies dealing with sharp PV fronts in the RSW dynamics.

The most striking results is a strong cyclone-anticyclone asymmetry in the wave frequency. According to the spatio-temporal plots, the oscillation is faster for the positive PV anomaly ([Figure 27\(b\)](#)) in comparison with the negative PV anomaly ([Figure 27\(a\)](#)). Indeed, if we measure the relative fluctuations of the upper layer thickness at the center ( $r = 0$ ), the frequency is sub-inertial ( $\omega/f \simeq 0.7$ ) in the anticyclonic PV patch while an inertial ( $\omega \simeq f$ ) frequency is found in the cyclonic PV patch ([Figure 28](#)).

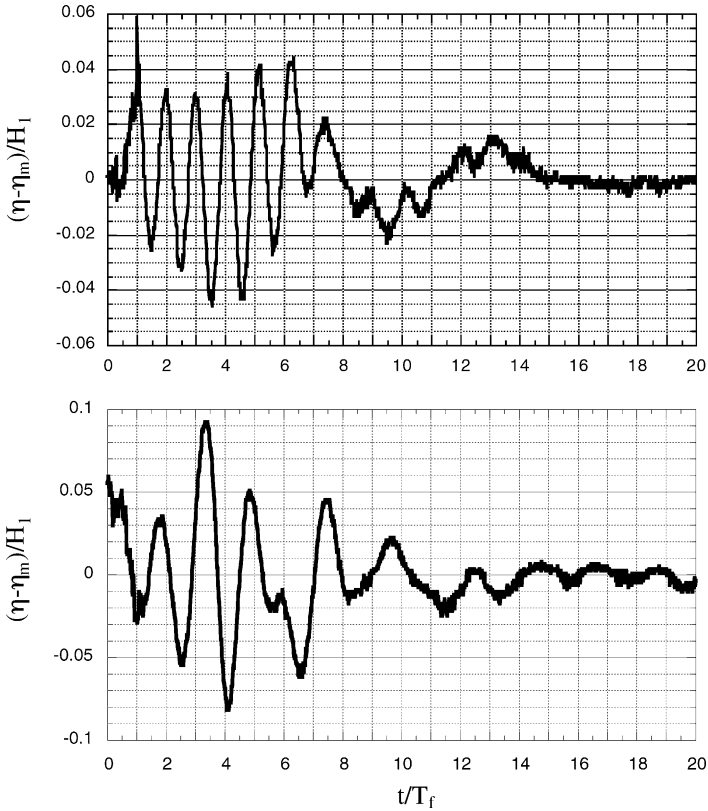


Figure 28. Evolution of the relative amplitude of the upper layer thickness at the center ( $r = 0$ ) of the initial height anomaly. The case of a cyclonic (anticyclonic) PV-patch is displayed in the upper (lower) panel.

In the rotating shallow-water configuration, the apparition of sub-inertial modes ( $\omega \leq f$ ) corresponds to trapped modes in other words, these modes must have an evanescent structure outside the PV-patch. If the relative vorticity is strong enough, a finite number of trapped modes could appear in anticyclonic vorticity region only (Kunze, 1985; Klein and Treguier, 1993; Young and BenJelloul, 1997; Llewellyn Smith, 1999; Plougonven and Zeitlin, 2005). The present experiment shows, for the first time in laboratory, the existence of sub-inertial modes within an anticyclonic PV-patch. However, according to Figure 28, these modes have a finite lifetime. Unlike, the long-lived trapped modes these sub-inertial waves probably radiate their energy to the lower layer. According to Figure 28, there is no cyclone-anticyclone asymmetry in the life time of the inner wave modes. Besides, according to the spatio-temporal graph displayed in Figure 27, the char-

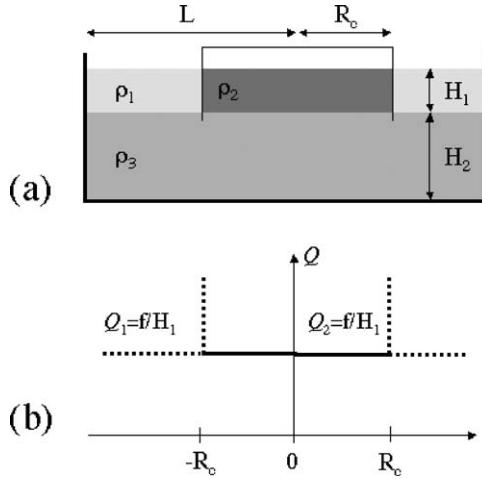


Figure 29. Experimental three-layer setup (a) and initial distribution of the potential vorticity (b).

acteristic size of the inner wave structure, both the cyclonic (inertial) and the anticyclonic (sub-inertial) one, decays with time. This is a signature of dispersive effects, which could be induced by the high value of the wave aspect ratio  $\alpha^{(2)} = H_2/L \simeq 10$  in the lower layer.

### 3.3. Uniform PV front

#### 3.3.1. Initial state and experimental configuration

The geostrophic adjustment of a motionless horizontal density gradient generally leads to a baroclinic tilted front corresponding to a simplified model of synoptic atmospheric fronts. However, recent studies (Ou, 1984; Blumen and Wu, 1995; Kalashnik, 2004; Plougonven and Zeitlin, 2005) have shown that even if the initial unbalanced state is smooth, a well defined continuous adjusted state may no longer exist. Indeed, for the case of uniform potential vorticity when the horizontal density gradient is sharp enough the steady adjusted solution exhibits discontinuities in both the density and the velocity field when the front outcrop the top or the bottom boundary.

We use a three layer setup to study the adjustment of an uniform PV front (Figure 29(a)). Two upper fluid layers having different density  $\rho_1$  and  $\rho_2$  but the same thickness  $H_1$  are initially separated by a bottomless cylinder. A third deep and dense lower layer acts as a neutral layer which separates the thin upper layers from the bottom boundary. According to the small thickness parameter  $\delta = 0.125$  and the weak motion in the lower layer we assume that two upper layers follows the reduced-gravity RSW equations. Hence, if the upper layers have exactly the

1 same thickness, the initial PV distribution is uniform and have the same value 1  
 2 inside ( $r < R_c$ ) and outside ( $r > R_c$ ) the cylinder (Figure 29(b)). However, as 2  
 3 for the warm-core lens configuration, the PV distribution exhibit a singularity at 3  
 4  $r = R_c$  for both the inner layer  $\rho_2$  and the outer layer  $\rho_1$  due to the vanishing of 4  
 5 the layer thickness. 5

6 We can define two baroclinic deformation radius namely:  $R_d =$  6  
 7  $\sqrt{((\rho_2 - \rho_1)/\rho_2)gh}/f$  related to the tilted density interface between the two 7  
 8 upper layers,  $R_D = \sqrt{((\rho_3 - \rho_2)/\rho_3)gh}/f$  related to the horizontal density 8  
 9 interface between the upper layers and one barotropic deformation radius corre- 9  
 10 sponding to the dense bottom layer  $R_B = \sqrt{gH}/f \simeq 1$  m. The density difference 10  
 11 between the layers ( $\rho_2 - \rho_1 = 3\text{--}25 \text{ g l}^{-1}$ ;  $\rho_3 - \rho_2 \simeq 100 \text{ g l}^{-1}$ ) were adjusted, 11  
 12 in the present experiment, in order to get  $R_d = 2\text{--}3 \text{ cm} \ll R_D \simeq 12 \text{ cm}$ . Besides, 12  
 13 the size of the rotating tank  $L = 45 \text{ cm}$  was large enough ( $L \gg R_c \geq R_d$ ) to 13  
 14 neglect side wall effects. More details on the experimental procedure are given in 14  
 15 (Mitkin, Stegner, Zeitlin and Pichon, 2006). 15  
 16

### 17 3.3.2. Dynamical stages 17

18 Several dynamical stages were observed during the adjustment process. Just after 18  
 19 the withdrawal of the separating cylinder, the inner dense fluid spreads radially 19  
 20 at the bottom interface. During this very initial stage, the flow exhibits strong 20  
 21 three-dimensional motions (Figure 30(b)) identical to those in a gravity current's 21  
 22 head (Paterson, Simpson, Dalziel and van Heijst, 2006). At this stage horizontal 22  
 23 vorticity is generated at the interface between the inner and the outer upper fluid 23  
 24 layers. After half of the inertial period the radial tilting of the density front is 24  
 25 stopped and a reverse flow occurs. Then, in about one inertial period this tilted 25  
 26 baroclinic front reaches an equilibrium characterized by an oscillating mean state. 26  
 27 Theses oscillations can be seen in the fluctuations of the extremal positions  $r_{\text{in}}$  and 27  
 28  $r_{\text{out}}$  of the tilted front (Figures 30(c) and (d)). At longer time ( $t = 5 - 10T_f$ ) this 28  
 29 tilted front experiences a large-scale baroclinic instability. The initial volume of 29  
 30 dense fluid looses its axial symmetry and splits in two vortices which move away 30  
 31 from the center of the tank. Hence, the vertical laser sheet does not capture the 31  
 32 central cross-section of the density field any more (Figure 30(e)). 32  
 33

### 34 3.3.3. Rotating shallow-water predictions 34

35 We assume here that: viscosity and dissipative effects are negligible ( $Re \gg 1,$  35  
 36  $E_k \ll 1$ ); each layer follows the rotating shallow-water dynamics ( $\alpha \ll 1$ ); top 36  
 37 and bottom boundary conditions are free-slip and rigid lid ( $\delta \ll 1, Bu^* \gg 1$ ). 37  
 38 Under these assumptions, the geostrophic adjustment of the density front is now 38  
 39 controlled by a single parameter, namely the Burger number  $Bu$ . 39  
 40

41 We look here for an axisymmetric steady state, solution of the RSW equations 41  
 42 in both the light outer layer 1 and the dense inner layer 2. For simplicity, we 42

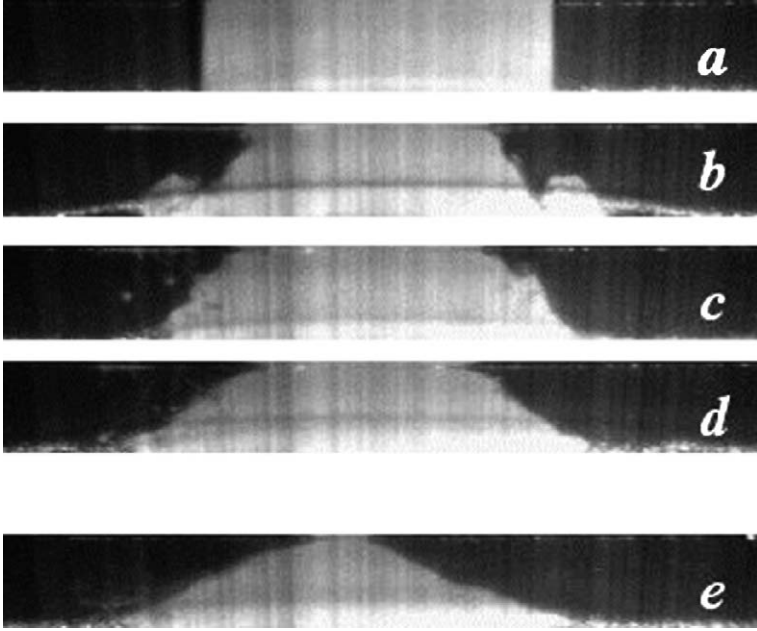


Figure 30. Vertical cross-section of the density front between the inner layer  $\rho_2$  (white region) and the outer layer  $\rho_1$  (dark region) visualized by LIV. These snapshots were taken at  $t = 0$  (a),  $t = 0.5T_f$  (b),  $t = T_f$  (c),  $t = 1.5T_f$  (d) and  $t = 5T_f$  (e) where  $T_f = 2\pi/f = 5$  s is the inertial period. This experiment corresponds to  $r_c = R_c/R_d = 2.1$  ( $Bu = 0.22$ ;  $\alpha = 1$ ).

neglect the cyclostrophic terms in the horizontal momentum equations. Such approximation is valid when  $R_c \gg R_d$ . In this case, the steady state satisfies an exact geostrophic balance and therefore using the pressure continuity at the interface we get

$$v_1 - v_2 = \partial_r \eta \quad (54)$$

where  $\eta$  is the dimensionless thickness of the inner layer 2. The Lagrangian PV conservation leads to a constant PV value for all fluid parcels in both layers:

$$Q_1(r \geq r_{\text{in}}) = \frac{1 + \zeta_1}{1 - \eta} = 1, \quad (55)$$

$$Q_2(r \leq r_{\text{out}}) = \frac{1 + \zeta_2}{\eta} = 1 \quad (56)$$

where  $\zeta_i = \frac{1}{r} \partial_r (r v_i)$  is the relative vorticity and  $r_{\text{in}}$  ( $r_{\text{out}}$ ) is the position of the upper (lower) intersection of the tilted density front with the top (bottom) boundary (Figure 31(b)). Note that, the boundary conditions  $\eta(r_{\text{in}}) = 1$  and  $\eta(r_{\text{out}}) = 0$  im-

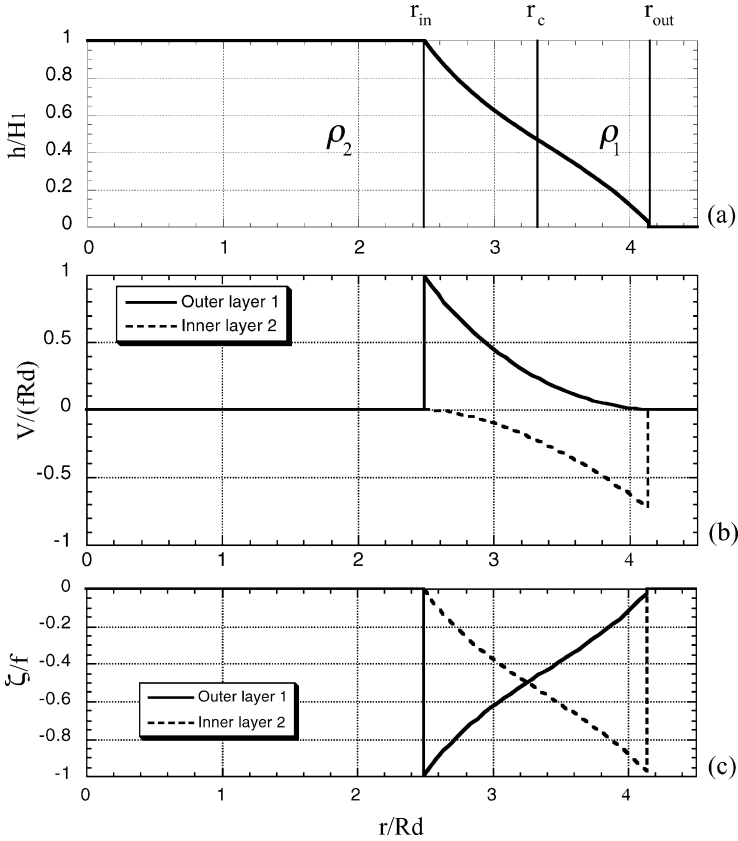


Figure 31. Density front (a), velocity (b) and vorticity (c) fields in the inner and outer layers of the adjusted steady-state according to the Rossby adjustment theory when  $r_c = 3.33$  ( $Bu = 0.09$ ).

ply a singularity in the PV field at the ends of both layers, even if the PV have the same constant value within the layers. Such singularities will be the source of discontinuities in the vorticity and velocity field of the adjusted state (Figures 31(b) and (c)). Then, the angular momentum conservation or the mass conservation gives both the same implicit relations between  $(r_{in}, r_{out})$  and the initial radius of the density front  $r_c = R_c/R_d = Bu^{-1/2}$ :

$$r_c^2 = r_{in}^2 + 2r_{in}v_1(r_{in}) = r_{out}^2 + 2r_{out}v_2(r_{out}). \quad (57)$$

Besides, outside of the region of the tilted front ( $r \leq r_{in}$  and  $r \geq r_{out}$ ) there is no radial displacement of fluid parcels. Therefore, the angular momentum conservation implies:

$$v_2(r \leq r_{in}) = v_1(r \geq r_{out}) = 0. \quad (58)$$

Then, according to equations (54), (55) and (56) we obtain the following system of linear equations:

$$\partial_{r^2}\phi + \frac{1}{r}\partial_r\phi - \left(2 + \frac{1}{r^2}\right)\phi = 0, \quad (59)$$

$$\partial_r(r\psi) = -r \quad (60)$$

where according to (57) and (58)  $\phi(r) = v_1 - v_2$  satisfies the following boundary conditions

$$\phi(r_{\text{in}}) = \frac{1}{2}\left(r_{\text{in}} - \frac{r_c^2}{r_{\text{in}}}\right); \quad \phi(r_{\text{out}}) = \frac{1}{2}\left(\frac{r_c^2}{r_{\text{out}}} - r_{\text{out}}\right) \quad (61)$$

and

$$\psi(r) = v_1(r) + v_2(r) = \frac{1}{2}\left(\frac{r_c^2}{r} - r\right). \quad (62)$$

For a given initial radius  $r_c = Bu^{-1/2}$  we can solve numerically (59) with (61) using a standard shooting method. An example of height, velocity and vorticity profiles in both layers are given in Figure 33 corresponding to  $r_c = 3.33$  ( $Bu = 0.09$ ). Due to the volume conservation in cylindrical geometry, the front displacement in the outer layer ( $r_c - r_{\text{in}}$ ) is not identical to the front displacement in the inner layer ( $r_{\text{out}} - r_c$ ). This leads to higher velocity amplitude in the outer layer (Figure 31(b)) according to (57). Even if the velocity field is strongly baroclinic (opposite direction in the upper and the lower layer) the vorticity is anticyclonic in both layers (Figure 31(c)) and reaches the extreme value  $\zeta = -f$  at both ends of the tilted density front.

### 3.3.4. Mean adjusted state

As for the previous cases, we use a time averaging over one inertial period, in order to separate the slow dynamics of the mean front and the fast dynamics of the oscillations. This temporal averaging filters out the fast dynamics on both the density front and the azimuthal velocity field.

According to Figure 32 the qualitative structure of the mean adjusted state measured in the experiment is in correct agreement with the geostrophic adjustment predicted by a simple two-layer RSW model. The averaged velocity profile, measured close to the upper free surface, is displayed in Figure 32(b). According to the standard inviscid adjustment model (solid line) the velocity is expected to be discontinuous in the outer layer at the upper edge of the front. This is obviously unrealistic in a physical system where dissipative processes occur. Hence, during the adjustment process a strong but continuous cyclonic shear is formed instead of the discontinuous velocity jump predicted by the inviscid theory. The width of this cyclonic shear is much smaller than the deformation radius ( $0.2 - 0.3R_d$ ).

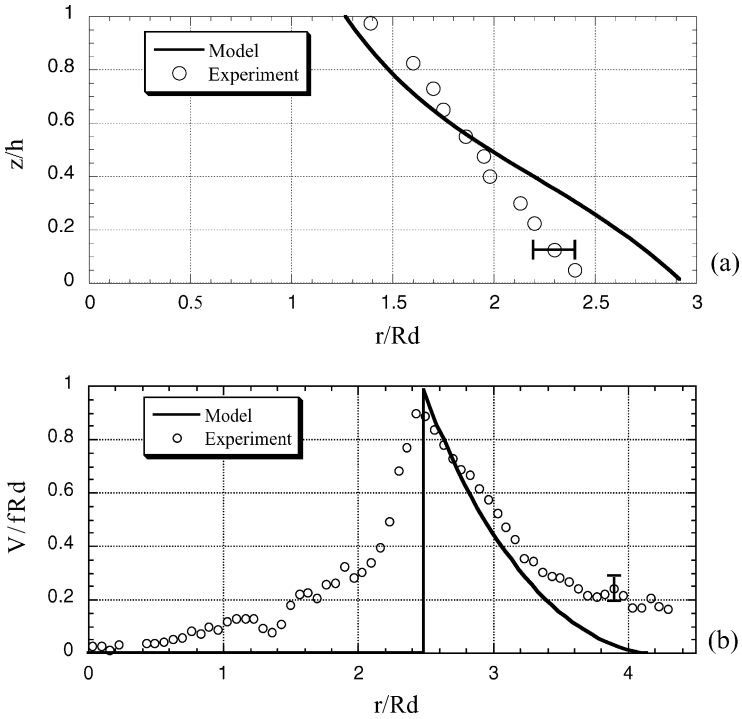


Figure 32. Comparison between the mean experimental adjusted state (dots) and the Rossby adjustment model (solid line). The vertical cross-section of the density profile (a) corresponds to  $R_c/R_d = 2.1$  ( $Bu = 0.22$ ) while the horizontal azimuthal velocity (b) measured close to the upper free surface corresponds to  $R_c/R_d = 3.33$  ( $Bu = 0.09$ ).

Besides, the vorticity in such thin shear layer exceeds the planetary vorticity ( $\zeta = 3 - 4f$  in Figure 32(b)) and may induce fast small-scale instabilities. However, the spatio-temporal resolution of the particle image velocimetry we used could hardly capture such small-scale instability patterns.

### 3.3.5. Small-scale instabilities

By means of LIV, we could visualize an horizontal cross-section of the sharp density gradient just below the free surface. The dynamical evolution of this sharp gradient is shown in Figure 33. After the release of the bottomless cylinder the upper front experiences a rapid radial contraction. Due to the angular momentum conservation, this radial contraction generates at the same time a strong azimuthal flow. During this very initial stage, small disturbances appears at the edge of the front. Using an edge detection image processing we could accurately measure the initial wavelength  $\lambda$  of this instability (Figure 33(b)). Due to its rapid growth

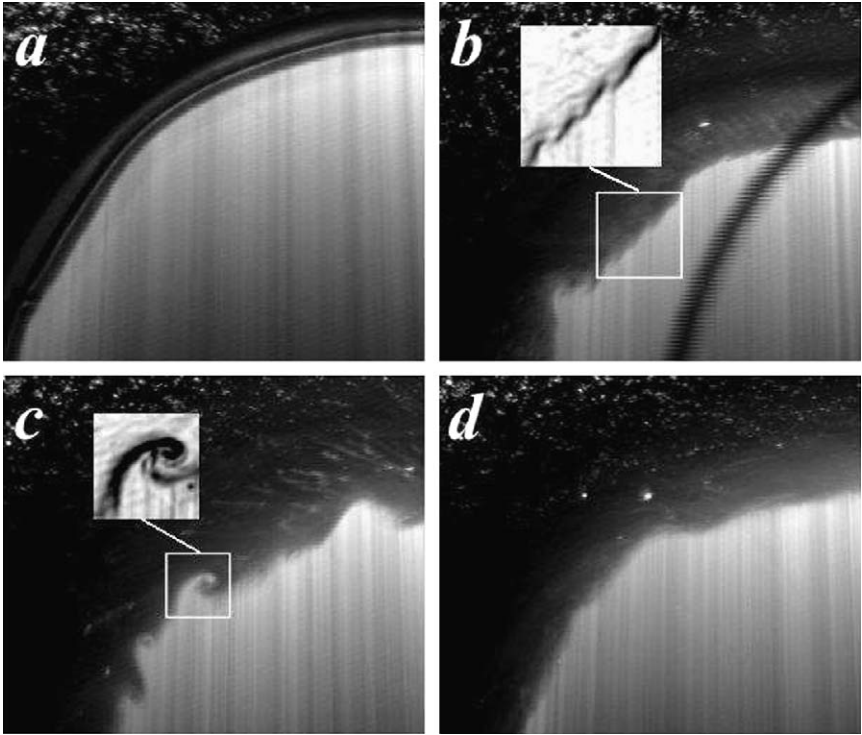


Figure 33. Visualization of small-scale disturbances at  $t = 0$  (a),  $t = 0.25T_f$  (b),  $t = 0.5T_f$  (c) and  $t = 0.75T_f$  (d) in a horizontal cross-section of the density front ( $Bu = 0.09$ ) just below the upper free surface. Local image processing of edge front detection are shown in (b) and (c), the black pixels corresponds to high values of the intensity gradient.

rate this instability is probably not affected by the rotation and the wavelength of the small-scale perturbations does not depend on the deformation radius (Mitkin, Stegner, Zeitlin and Pichon, 2006).

In the present case, unlike the outcropping lens configuration, no secondary instability occurs and the non-linear saturation of the initial perturbation leads to the formation of strong cusps and small cyclones appear according to Figure 33(c). Here again the size of these intense cyclones could be much smaller than the deformation radius and remain independent from this latter. These cat eye patterns look like a classical horizontal shear instability. Nevertheless, due to the baroclinic structure of the flow, the vertical extension of these small cyclones is limited and they should be formed preferentially at the top or the bottom edge of the density front. Besides, these vortices are transient features of the adjustment process. Indeed, after half an inertial period the front reaches his maximal contraction and the small cyclones disappear during the reverse oscillation (Figure 33(d)).

## 4. What do we learn from laboratory experiments?

Laboratory experiments can hardly reproduce the complex thermodynamics (moisture, turbulent boundary layer convection, evaporation, air-sea fluxes...) and the wide range of dynamical regimes ( $Re \gg 1$ ;  $\delta \ll 1$ ) encountered in the atmosphere or the ocean. However, the physical modeling of rotating shallow water flows is very useful especially for the geostrophic adjustment process, where several dynamical features occur on various temporal and spatial scales.

Previous laboratory experiments have shown that the geostrophic adjustment is a rapid process (Ungarish, Hallworth and Huppert, 2001; Bouruet-Aubertot and Linden, 2002; Rubino and Brandt, 2003; Thivolle-Cazat, Sommeria and Galmiche, 2005). But very few studies investigate the characteristic time of this process especially when strong wave activity is present. According to all the cases we studied, a mean adjusted state is reached after approximately one or two inertial periods  $T_f$ . The rapidity of the geostrophic adjustment does not depend on the size or the amplitude of the initial unbalance state. The so-called mean state is obtained from a simple time-averaging over  $T_f$ , in order to filter out the fast wave motion. We say that this averaged state reaches an equilibrium (i.e. gets adjusted) when its temporal evolution remains small in comparison with the characteristic wave frequency. Hence, even if a strong wave activity is present in the initial region of unbalance, the mean flow could nevertheless be adjusted. This experimental observation is in good agreement with the standard hypothesis of dynamical splitting between the fast ( $\varepsilon \geq 1$ ) and the slow ( $\varepsilon \ll 1$ ) component of motion. In the limit of small Rossby numbers, the asymptotic analysis shows that the slow component of motion does not feel the fast one (Chapter 2). Therefore, the existence of a mean adjusted state does not depend on the presence (or not) of fast wave motion. Besides, the experimental results for both the warm-core lens configuration and the uniform PV front configuration showed that a mean adjusted state could be extracted from the wave motion with a simple time-averaging even for finite Rossby numbers. Hence, according to the whole set of experiments, the fast component of motion seems to have only a weak influence (if any) on the evolution of the mean adjusted state for a wide range of parameters ( $Ro < 1$ ,  $Bu \simeq 0.1-10$ ,  $-0.5 < \lambda < 0.5$ ).

These two-layer or three-layer experiments also show that the PV conservation remains robust even if the initial state does not satisfy the assumptions of the rotating shallow-water model. Indeed, in almost all the cases, three-dimensional and non-hydrostatic motions (shocks or gravity current head) could occur in the early stage of adjustment. Nevertheless, the prediction of the RSW model based on the PV conservation gives a correct estimation of the mean adjusted state. A very good agreement is found for the cases of cyclonic PV front when there is no outcropping. However, the PV conservation could be locally broken in the case of outcropping fronts when the initial PV profile exhibits a singularity (i.e.

1 the layer thickness vanish at a given position). In such case, all the experiments 1  
 2 exhibit transient and three-dimensional instabilities localized around the PV sin- 2  
 3 gularity. These instabilities are an efficient mechanism of turbulent dissipation 3  
 4 which rapidly cascades energy toward small scales in the frontal region. For the 4  
 5 uniform PV front configuration, small and intense cyclones are formed in a very 5  
 6 short time ( $\sim 0.5T_f$ ) during the adjustment of a large scale anticyclonic front. The 6  
 7 rapid formation of these structures, which are much smaller than the deformation 7  
 8 radius, were not predicted by the standard scenario of adjustment and they could 8  
 9 hardly be captured by standard numerical simulations which have limited spatial 9  
 10 resolution. The laboratory experiment shows here a new mechanism of formation 10  
 11 of small and intense structures within a large-scale synoptic front. 11

12 The relaxation of any unbalanced initial state in a rotating shallow-water model 12  
 13 will always leads to the emission of Poincaré waves (away from lateral bound- 13  
 14 aries). In a real laboratory experiment, both hydrostatic and non-hydrostatic 14  
 15 waves could be emitted at the same time and the spectral gap between the fast 15  
 16 and the slow component of motion could then be filled. However, according 16  
 17 to our experiments and previous studies (Bouruet-Aubertot and Linden, 2002; 17  
 18 Rubino and Brandt, 2003; Thivolle-Cazat, 2003) the energy released to the wave 18  
 19 modes during the adjustment is mainly concentrated around the inertial frequency. 19  
 20 A significant wave activity remain for a long time (several inertial period) inside 20  
 21 both the cyclonic and the anticyclonic structures even if the mean steady state is 21  
 22 already adjusted. For some specific configuration the anticyclonic structure may 22  
 23 exhibit sub-inertial oscillations. Such wave activity is in good agreement with the 23  
 24 RSW model predictions (Chapters 2 and 3) and confirm the dynamical splitting 24  
 25 between the fast waves and the slow adjusted motion. However, the inertia-gravity 25  
 26 waves detected in the experiment have a dispersive behavior due to the finite value 26  
 27 of the aspect ratio parameter  $\alpha$ . This could explain why we did not see any 27  
 28 evidence of the wave breaking events predicted in the RSW framework (Chapter 3). 28  
 29 The small scale shocks we observed in the very initial stage of adjustment seems 29  
 30 to be due to a local overturning event rather than a propagating wave leading to 30  
 31 breaking. 31  
 32 32  
 33 33

34 **Acknowledgements** 34

35 The work presented in this chapter was done in collaboration with V. Mitkin, 35  
 36 P. Bouruet-Aubertot and T. Pichon which are gratefully acknowledge. 36  
 37 37

38 **Uncited references** 38

39 (Hart, 2000) (Obukhov, 1949) (Reznik, Zeitlin and BenJelloul, 2001) (Rossby, 39  
 40 1937) (Williams, Read and Haine, 2003) (Zeitlin, Reznik and Ben Jelloul, 2003) 40  
 41 41  
 42 42

## References

- Adrian, R.J., 2005. Twenty years of particle image velocimetry. *Experiments in Fluids* 39, 159–169.
- Afanasyev, Ya.D., Peltier, W.R., 1998. Three dimensional instability of anticyclonic swirling flow in rotating fluid: Laboratory experiments and related theoretical predictions. *Phys. Fluids* 10, 3194.
- Afanasyev, Y.D., Rhines, P.B., Lindahl, E.G., 2006. Altimetric imaging velocimetry: investigation of emission of inertial and Rossby waves by baroclinally unstable flows. *J. Fluid Mech.*, submitted for publication.
- Blumen, W., Wu, R., 1995. Geostrophic adjustment: frontogenesis and energy conservation. *J. Phys. Oceanogr.* 58, 2180–2195.
- Bouruet-Aubertot, P., Linden, P.F., 2002. The influence of the coast on the dynamics of upwelling fronts. Part I: Laboratory experiments. *Dynam. Atmos. Oceans* 36, 153–173.
- Bracco, A., McWilliams, J.C., Murante, G., Provenzale, A., Weiss, J.B., 2000. Revisiting freely decaying two-dimensional turbulence at millennial resolution. *Phys. Fluids* 12, 2931.
- Carnevale, G.F., Kloosterziel, R.C., van Heijst, G.J.F., 1991. Propagation of barotropic vortices over topography in a rotating tank. *J. Fluid Mech.* 233, 119–139.
- Cushman-Roisin, B., Sutyrin, G.G., Tang, B., 1992. Two-layer geostrophic dynamics. Part I: Governing equations. *J. Phys. Oceanogr.* 22, 117.
- Fincham, A.M., Spedding, G.R., 1997. Low cost, high-resolution DPIV for measurement of turbulent fluid flow. *Experiments in Fluids* 23, 449–462.
- Flor, J.B., Eames, I., 2002. Dynamics of monopolar vortices on a topographic beta-plane. *J. Fluid Mech.* 456, 353–376.
- Gill, A.E., 1982. *Atmosphere Ocean Dynamics*. Academic Press, San Diego, CA.
- Greenspan, G.P., 1968. *The Theory of Rotating Fluids*. Cambridge Univ. Press, Cambridge, UK.
- Griffiths, R.W., Linden, P.F., 1981. The stability of vortices in a rotating, stratified fluid. *J. Fluid Mech.* 105, 283–316.
- Hart, D.P., 2000. PIV errors correction. *Experiments in Fluids* 29, 13–22.
- Hart, J.E., Kittelman, S., 1986. A method for measuring interfacial wave fields in the laboratory. *Geophys. Astrophys. Fluid Dynam.* 36, 179–185.
- Hart, J.E., 2000. A note on nonlinear corrections to the Ekman layer pumping velocity. *Phys. Fluids* 12, 131–135.
- Holford, J.M., Dalziel, S.B., 1996. Measurements of layer-depth in a two-layer flow. *Appl. Sci. Res.* 56, 191–207.
- Johnson, J.A., 1963. Stability of shearing motion in rotating fluid. *J. Fluid Mech.* 17, 337.
- Kalashnik, M.V., 2004. Geostrophic adjustment and frontogenesis in a continuously stratified fluid. *Dynam. Atmos. Oceans* 38, 1–37.
- Klein, P., Treguier, A.M., 1993. Dispersion of wind-induced inertial waves by a barotropic jet. *J. Marine Res.* 53, 1–22.
- Kuo, A.C., Polvani, L.M., 2000. Nonlinear geostrophic adjustment, cyclone/anticyclone asymmetry, and potential vorticity rearrangement. *Phys. Fluids* 12, 1087–1100.
- Kunze, E., 1985. Near-inertial wave propagating in geostrophic shear. *J. Phys. Oceanogr.* 23, 1897–1915.
- Llewellyn Smith, S., 1999. Near-inertial oscillations of a barotropic vortex trapped modes and time evolution. *J. Phys. Oceanogr.* 29, 747–761.
- Mahalov, A., Pacheco, J.R., Voropayev, S.I., et al., 2000. Effects of rotation on fronts of density currents. *Phys. Lett. A* 270, 149–156.
- Masuda, A., Marubayashi, K., Ishibashi, M., 1990. A laboratory experiment and numerical simulation of an isolated barotropic eddy in a basin with topographic  $\beta$ -plane. *J. Fluid Mech.* 213, 641–655.
- Mitkin, V., Stegner, A., Zeitlin, V., Pichon, T., 2006. Generation of small-scale and intense cyclones during the geostrophic adjustment of large-scale fronts. *J. Fluid Mech.*, submitted for publication.

- 1 Nezlin, M.V., Snezhkin, E.N., 1993. Rossby Vortices, Spiral Structure, Solitons. Springer-Verlag, 1  
 2 Berlin/New York. 2
- 3 Nycander, J., 1993. The difference between monopole vortices in planetary flows and laboratory ex- 3  
 4 periments. *J. Fluid Mech.* 254, 561–577. 4
- 5 Obukhov, A.M., 1949. On the question of the geostrophic wind. *Izv. Akad. Nauk SSSR Ser.* 5  
 6 *Geograph.–Geophys.* 13, 291–306. 6
- 7 Ou, H.W., 1984. Geostrophic adjustment: a mechanism for frontogenesis. *J. Phys. Oceanogr.* 14, 994– 7  
 8 1000. 8
- 9 Paterson, M.D., Simpson, J.E., Dalziel, S.B., van Heijst, G.J.F., 2006. Vortical motion in the head of 9  
 10 an axisymmetric gravity current. *Phys. Fluids* 18, 046601. 10
- 11 Pedlosky, J., 1987. *Geophysical Fluid Dynamics*. Springer-Verlag, Berlin/New York. 11
- 12 Perret, G., Stegner, A., Farge, M., Pichon, T., 2006. Cyclone-anticyclone asymmetry of large-scale 12  
 13 wakes in the laboratory. *Phys. Fluids* 18, 036603. 13
- 14 Plougonven, R., Zeitlin, V., 2005. Lagrangian approach to geostrophic adjustment of frontal anomalies 14  
 15 in a stratified fluid. *Geophys. Astrophys. Fluid Dynam.* 99 (2), 101–135. 15
- 16 Reznik, G.M., Zeitlin, V., BenJelloul, M., 2001. Nonlinear theory of geostrophic adjustment. Part I. 16  
 17 Rotating shallow-water model. *J. Fluid Mech.* 491, 207–228. 17
- 18 Rhines, P.B., 2006. Jets and orography: Idealized experiments with tip-jets and Lighthill blocking. 18  
 19 *J. Atmos. Sci.*, submitted for publication. 19
- 20 Rhines, P.B., Lindahl, E.G., Mendez, A.J., 2006. Optical altimetry: a new method for observing ro- 20  
 21 tating fluids with applications to Rossby and inertial waves on a polar  $\beta$ -plane. *J. Fluid Mech.*, 21  
 22 submitted for publication. 22
- 23 Rossby, C.G., 1937. On the mutual adjustment of pressure and velocity distribution in simple current 23  
 24 systems. *Int. J. Marine Res.* 1, 15–28. 24
- 25 Rubino, A., Brandt, P., 2003. Warm-core eddies studied by laboratory experiments and numerical 25  
 26 modeling. *J. Phys. Oceanogr.* 33 (2), 431–435. 26
- 27 Stegner, A., Bouruet-Aubertot, P., Pichon, T., 2004. Nonlinear adjustment of density fronts. Part 1. 27  
 28 The Rossby scenario and the experimental reality. *J. Fluid Mech.* 502, 335–360. 28
- 29 Stegner, A., Pichon, T., Beunier, M., 2005. Elliptical-inertial instability of rotating Karman vortex 29  
 30 streets. *Phys. Fluids* 17, 066602. 30
- 31 Stegner, A., Zeitlin, V., 1998. From quasi-geostrophic to strongly nonlinear monopolar vortices in a 31  
 32 paraboloidal shallow-water experiment. *J. Fluid Mech.* 356, 1–24. 32
- 33 Teinturier, S., Stegner, A., Viboud, S., Didelle, H., Ghil, M., 2006. Inertial instability of von Karman 33  
 34 street in a rotating shallow-water layer. *Dynam. Atmos. Oceans*, submitted for publication. 34
- 35 Thivolle-Cazat, E., 2003. PhD Thesis, University Joseph Fourier, Grenoble. 35
- 36 Thivolle-Cazat, E., Sommeria, J., Galmiche, M., 2005. Baroclinic instability of two-layer vortices in 36  
 37 laboratory experiments. *J. Fluid Mech.* 544, 69–97. 37
- 38 Ungarish, M., Hallworth, M.A., Huppert, H.E., 2001. Axisymmetric gravity currents in a rotating 38  
 39 system: Experimental and numerical investigations. *J. Fluid Mech.* 447, 1–29. 39
- 40 Ungarish, M., Huppert, H.E., 1998. The effect of rotation on axisymmetric gravity currents. *J. Fluid* 40  
 41 *Mech.* 362, 17–51. 41
- 42 Vallis, B., 2006. *Atmospheric and Oceanic Fluid Dynamics*. Cambridge Univ. Press, Cambridge, UK. 42  
 van de Konijnenberg, J.A., Nielsen, A.H., Rasmussen, J.J., Stenum, B., 1999. Shear-flow instability in 42  
 a rotating fluid. *J. Fluid Mech.* 387, 177–204.
- Yanase, S., Flores, C., Metais, O., Riley, J., 1993. Rotating free-shear flows. I. Linear stability analysis. 37  
*Phys. Fluids* 5 (11), 2725–2737.
- Young, W.R., BenJelloul, M., 1997. Propagation of near-inertial oscillations through a geostrophic 39  
 flow. *J. Marine Res.* 55, 735–766.
- Williams, P.D., Read, P.L., Haine, T.W.N., 2003. Spontaneous generation and impact of 40  
 inertia–gravity waves in a stratified, two-layer shear flow. *Geophys. Res. Lett.* 30, 22555, 41  
 doi:10.1029/2003GL018498. 42

- 1 Williams, P.D., Read, P.L., Haine, T.W.N., 2004. A calibrated, non-invasive method for measuring 1  
2 the internal interface height field at high resolution in the rotating, two-layer annulus. *Geophys.* 2  
3 *Astrophys. Fluid Dynam.* 98, 453–471. 3  
4 Zavala Sanson, L., van Heijst, G.J.F., 2000. Nonlinear Ekman effects in rotating barotropic flows. 4  
5 *J. Fluid Mech.* 412, 75–91. 5  
6 Zeitlin, V., Reznik, G.M., Ben Jelloul, M., 2003. Nonlinear theory of geostrophic adjustment. Part 2. 6  
7 Two-layer and continuously stratified primitive equations. *J. Fluid Mech.* 491, 207–228. 6  
8 7  
9 8  
10 9  
11 10  
12 11  
13 12  
14 13  
15 14  
16 15  
17 16  
18 17  
19 18  
20 19  
21 20  
22 21  
23 22  
24 23  
25 24  
26 25  
27 26  
28 27  
29 28  
30 29  
31 30  
32 31  
33 32  
34 33  
35 34  
36 35  
37 36  
38 37  
39 38  
40 39  
41 40  
42 41  
42 42